Evaluation of the First Generation Dual-purpose Coatings for SiC Cladding

**Nuclear Technology
Research and Development**

SUMMARY

The loss of coolant and station blackout at the Fukushima Daichi nuclear power station highlighted the need to improve the safety margins of current and future Light Water Reactors (LWRs). Accident Tolerant Fuel (ATF) development is designed to find solutions to mitigate or prevent such events through improvement of fuels and fuel cladding. One promising ATF concept is the replacement of zirconium-based alloy cladding with silicon carbide (SiC) fiber-reinforced SiC matrix (SiC_f-SiC) composites, due to the inherent accident resistant features of SiC. However, during normal operations, SiC corrodes in reactor coolant potentially at an unacceptable rate. In addition, it is likely for the SiC-based cladding to undergo microcracking under an applied stress, which potentially degrades the hermeticity.

To address both challenges, a dual-purpose barrier coating for SiC cladding is proposed by Oak Ridge National Laboratory (ORNL). Coating technologies and deposited materials were the key focus of the research. The selected materials for coatings are of compositions that previously demonstrated good performance for metallic cladding systems in LWRs (Cr, CrN, Zr, etc.). However, the technologies to deposit these materials require significant effort to integrate with a SiC substrate. Three technologies at varying readiness levels were pursued with industry collaborators. These were, respectively, electrochemical deposition, vacuum plasma spray (VPS) and cathodic arc physical vapor deposition (PVD). While the PVD technology required minimal adaptation for any substrate, electrochemical and VPS coatings needed extensive development for compatibility with the SiC substrate.

The present report documents the evaluation of the first-generation coatings by convergent metrics of successful processing, morphology, mechanical properties, radiation stability, and especially, corrosion and gas-tightness. The electrolytic coatings are to date unsuccessful due to cracking after processing and VPS coatings could not deposit a suitable phase of Zr. From preliminary hermeticity or corrosion evaluations, these two technologies requires significantly more effort to demonstrate the technical feasibility. The PVD coatings appear to be viable and showed absence of significant changes after neutron irradiation in a chemically inert environment and have been successful after exposure to autoclave environments. Thus, PVD technologies are currently the leading candidates for future efforts on integrated development for barrier coatings for SiC cladding.

CONTENTS

FIGURES

TABLES

ACRONYMS

ASTM – American Society for Testing and Materials
ATF – Accident Tolerance Fuel
BSE – Back Scatter Electron (Microscopy)
BWR – Boiling Water Reactor
CVD – Chemical Vapor Deposition
CVI – Chemical Vapor Infiltration
DoE – Department of Energy
EFPD - Effective Full Power Days
HCL – Hydrothermal Corrosion Laboratory
LAMDA – Low Activation Materials Development and Analysis
LWR – Light Water Reactor
MIT - Massachusetts Institute of Technology
NEO – NEO Knoxville
NIST – National Institute of Standards and Technology
NRL - Nuclear Reactor Laboratory
ORNL – Oak Ridge National Laboratory
PP – Plasma Processes
PVD – Physical Vapor Deposition
PWR – Pressurized Water Reactor
PyC – Pyrolytic Carbon
RP – Richter Precision
SEM – Scanning Electron Microscopy
SiC_f-SiC – Silicon Carbide fiber-reinforced Silicon Carbide composite
SS – Stainless Steel
TM – Techmetals
VPS – Vacuum Plasma Spray
XRD – X-Ray Diffraction

EVALUATION OF THE FIRST GENERATIONAL DUAL-PURPOSE COATINGS FOR SIC CLADDING

1. INTRODUCTION

The events at Fukushima Daichi nuclear power station in 2011 resulted in a drive to improve the safety of Light Water Reactors (LWRs). Accident Tolerant Fuels (ATFs) are a key part of this effort and are intended to provide an engineering control for reactor accidents. Ideally, ATFs mitigate the need for operator input and extend the safety margin for operator response. A secondary but no less important purpose for ATFs is to integrate into the LWR fleet via "drop-in replacement" without significant modification to existing reactor structures.[1]

One structure of the reactor that is under ATF development is replacement of cladding, substituting zircaloy-type alloys with silicon carbide (SiC) fiber reinforced SiC matrix (SiC_f-SiC) composites. Due to its high mechanical strength and relatively inert behavior in high temperature steam[2], the composite fuel cladding eliminates the zirconium-steam reaction and may mitigate or prevent radionucleotide release. However, two key feasibility issues of SiC_f-SiC cladding have been identified. These are, respectively, the unique radiation stress state that may introduce cracks and consequently compromise hermeticity [3-6] and aggravated hydrothermal corrosion in LWR coolant.[7-9] A coating is proposed as a metallic environmental barrier coating and hermetic seal.[10]

Current SiC cladding is based on the CVD/I (Chemical Vapor Deposition/Infiltration) process on SiC fiber (SiC_f) tube preforms. A coating can be deposited during this process. However, development of an appropriate deposition technology has the advantage of being used on alternative SiC materials, which may be powder-processed, or sealed fuel rod end-caps. To this end, three coating technologies were investigated, and each coating technology had specific topcoat (coolant facing) corrosion-resistant materials.

Depositing a metal resistant to corrosion is intrinsically challenging since the process must deposit the metal in ground-state. The process must provide a reducing environment, sequester the metal ion against O^{2-} or alter in-situ the anodic potential of the substrate. Vacuum Plasma Spray technology pursued a Zircaloy-2 powder spray under inert gas. Electrochemical techniques intended Cr as the coolant-facing material and altered the potential of the cladding to reduce the metal from solution onto the substrate. Physical Vapor Deposition evaporated metallic targets of Ti and Cr in vacuum or nitrogen gas, which electrically accelerated Cr, Cr-N and Ti-N on the cladding. These materials, when processing and microstructure was controlled, have demonstrated promising performance history in reactor coolant [11, 12] or simulated coolant [13-15]

However, ad hoc demonstration of a deposit of specific composition does not define a coating; by definition, the substrate-deposit interface must be maintained.[16] The competition between interface cohesion and processing-microstructural evolution leads to stresses. For example, in some coatings, densification (volume shrinkage), phase changes and thermal evolution can all occur while an interface is constrained. In metals deposited on ceramics, significant compressive

stresses typically occur where the metal has a higher coefficient of thermal expansion than SiC. Consequently, microscopic and macroscopic effects, such as delamination, microcracking and channeling can often define feasibility of a coating-substrate system. A more detailed discussion of the interface stresses, interface compatibility and strategies with bond coatings can be found in "M3FT-16OR020202113, ORNL-TM-2016-332 - Examination of Hybrid Metal Coatings for Mitigation of Fission Product Release and Corrosion Protection of LWR SiC/SiC". The only successful first-generation coatings were those that could mitigate deposition stresses, rather than demonstrate corrosion or hermetic performance.

This report documents the first-generation coatings and evaluates their integrated radiation resistance, the corrosion performance of the topcoat and hermeticity tests. A brief overview of the processing is also included. The more successful coatings typically had intrinsic substrate compatibility. Physical Vapor Deposition by cathodic arc appeared to be successful in all tests and provided the bulk of results that demonstrated a coating technology promising for corrosion protection and hermetic sealing of potential SiC cladding.

Section 2 briefly describes morphology, characterization and derived properties of the coatings. Section 3 shows the results of mechanical testing via debonding and scratch indentation, photographs from irradiation of coated SiC coupons under inert gas environment and corrosion tests in simulated reactor coolant. A brief section of hermeticity testing of prototype cladding sections is included for the PVD coatings. Finally, Section 5 discusses the results and future directions being undertaken to ensure success of the program.

2. EXPERIMENTAL

2.1 SUBSTRATE AND COATING

The part to be coated, referred to as the substrate from here onward, was typically high purity, stoichiometric CVD SiC, CVI SiC$_f$-SiC composite with CVD SiC overcoat . Table 1 shows a comprehensive list of SiC plate and tube specimens used in the program and their use in irradiation, mechanical, corrosion and permeation testing.

Table 1 shows a significant effort to acquire materials that are simulated or actual substrates of nuclear grade SiC materials. Substrate preparation was conducted to remove surface contaminants, typical of preparation for chemical deposition methods.[17-20]

Briefly, SiC was cleaned with acetone, alkali and nitric acid, followed by etching. Etchants included HF, HSO$_3$F, Na$_2$CO$_3$ and NaOH. This etching was critical in providing adhesion for the coating because the surface roughness of machined or abraded CVD SiC is inadequate for deposition of bond coats. Etching was not required for Vacuum Plasma Spray (VPS) because the plasma preheats the substrate, ablates the surface and removes both surface oxides and regions of the substrate. For PVD coatings, the preparation of the substrate beyond hydrofluoric acid treatment did not appear to be necessary. After cleaning or etching, coupons and tubes were then sent to industrial vendors and collaborators for PVD and VPS coating.

Table 1. Coupons and cladding sections used in complete coating evaluations for SiC. OD stands for outer diameter of the tube.

Purpose	Size (mm)	Substrate material
Processing	25 x 5 x 2	Composite: Hi-Nicalon S/Hypertherm CVI SiC$_f$/SiC
Processing	All sizes	Monolith: Rohm and Haas CVD SiC
Irradiation	25 x 6 x 1	Composite: Tyranno SA3/Hypertherm CVI SiC$_f$/SiC
Irradiation	25 x 6 x (0.5, 1, 2)	Monolith: Rohm and Haas CVD SiC
Irradiation	25 x 8.5 (OD)	Composite tube: SiC$_f$, General Atomics CVI SiC$_f$/SiC
Scratch Test	25 x 6 x (0.5, 1, 2)	Monolith: Rohm and Haas CVD SiC
Debonding Test	14 x 14 x 3	Monolith: Rohm and Haas CVD SiC
Corrosion Test	25 x 6 x 1	Monolith: Rohm and Haas CVD SiC
Permeation Test	25 x 8.5 (OD)	Composite tube: various

However, electrolytic chromium needed a compatibility coating since SiC is non-conductive. At ORNL, either Ni or pyrolytic carbon (PyC) was deposited on etched SiC. PyC was deposited on coupons of CVD SiC and SiC$_f$-SiC composites using a fluidized bed reactor with acetylene/propylene as feedstock, as reported elsewhere.[21] A second compatibility coating based on Ni was investigated and discontinued.[10, 22, 23] After the compatibility coating was deposited, coupons and tubes were sent for electroplating.

Further details on vendor processing equipment and schematics can be found in "M3FT-16OR020202113, ORNL-TM-2016-332 - Examination of Hybrid Metal Coatings for Mitigation of Fission Product Release and Corrosion Protection of LWR SiC/SiC".

2.2 MICROSTRUCTURAL CHARACTERIZATION

Deposition thickness of all coatings was typically calculated by weight changes. Skeletal thickness (used for upper thickness measurements) was measured using micrometers calibrated using inspection gage blocks (Mituoyo 516-101-26). After plating, specimens were mounted and polished to 0.04 μm. Where specified, the coating thickness is based on optical microscopy and SEM imaging. Table 2 lists the expected thicknesses and composition of the deposits prior to rigorous characterization.

Table 2. Deposition technologies, source materials, expected phases and coating thickness on SiC.

Coating technology	Source material	Phases	Thickness (μm)
Electrolytic	Hexavalent chromium	C, Cr	10, 10
Vacuum Plasma Spray (VPS)	Zircaloy-2 powder	Zr$_x$Si$_y$, Zr, ZrC	<50
Physical Vapor Deposition (PVD)	Metallic target, gas (N$_2$)	CrN, TiN, Cr$_2$N	5-10
Physical Vapor Deposition (PVD)	Metallic target	Cr	<30

The coated SiC specimens were characterized by X-ray diffraction (XRD) using Cu Kα radiation using a D2 Phaser X-Ray Diffractometer (Bruker AXS) running at 30 kV and 30 mA. The samples were mounted on a zero-background (SiO2 Optical Grade from MTIXTI) XRD sample mount. Instrument profile for size-strain standard was determined by a NIST 660d LaB6, and the specimen displacement and zero error was calibrated by NIST 640b Si internal standard. SEM imaging of cross-section samples shown were analyzed using a JEOL6500F SEM.

2.3 MECHANICAL TESTING

Coated coupons were subjected to two sets of mechanical tests: debonding or pull-off test (by ASTM D4541) and scratch-indentation test (by ASTM E2546). The pull-off test for adhesion strength was conducted using pull stubs epoxy-bonded to the top coat. The epoxy mixture was Araldite, cured at 60°C for 12 hours prior to testing. Afterward, the pneumatic system locked around the head of a pull stub and applied force to remove it. Removal of the coating verified valid tests, and the debond strength was approximated using an imposed circle representing the area removed. Where a clear circle could not be identified, a square test area established a lower range.

Adaptation of the test for small irradiation coupons (5 mm test diameter) was conducted by reducing the size of the pull stub. Tests were cross-referenced with 10 mm pull stubs. The strength of the selected epoxy was verified by at least 10 pull-off tests, and coatings were assessed by a minimum of 5 tests in both 5/10 mm configurations. Figure 1 shows an optical micrograph of the interfaces between pull stub, epoxy and coating.
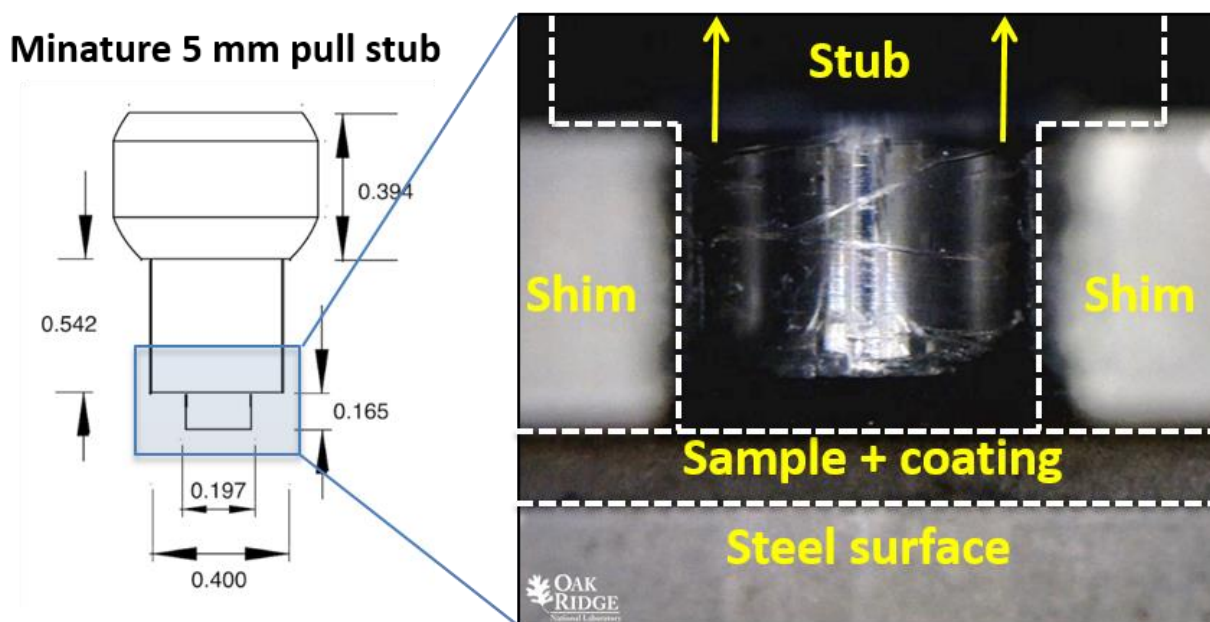
Figure 1. Schematic of modified 5 mm pull stubs adapted from ASTM D4541 and a cross-section view of the interface between pull-stub and sample/coating prior to test.

Debonding tests can adapt typical tensile test fixtures or use portable debonding systems. The mobility of debonding tests conducted by ASTM D4541 permits easy post-irradiation examination using the exact same equipment and can be used as an ad hoc "pass-fail" test. If several tests are conducted, a statistically detectable change in interface strength caused by irradiation may be discernable.

Scratch-indentation testing was conducted using a PB-1000 Micro/Macro Module (Nanovea, CA, USA) with a progressive load from 0.1 to 50N at 100N/min using a 120° diamond indentor of radius 100 μm. Figure 2(a) illustrates the instrument, while Figure 2(b) shows a schematic of the test. To understand the damage evolution, data such as acoustic emission, the coefficient of friction and change in depth are recorded.
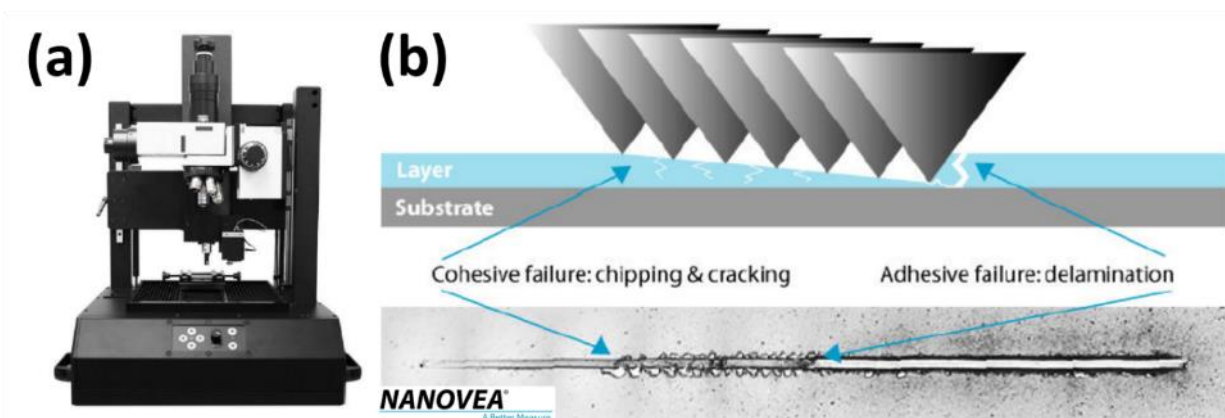
Figure 2. Scratch indentation test showing (a) module of the PB-1000 Macro/Micro-Scratch Tester (Nanovea, CA, USA) and (b) the schematic of the scratch indentation test, conducted with increasing progressive load. (Images courtesy of Nanovea, CA, USA)

Two specific load values are of interest. The first is Load at Cohesion Failure, which is typically an increase in acoustic emission and coefficient of friction that indicates the coating material has fractured or deforms significantly. The second is Load at Adhesion Failure, recognized by a change in all three data outputs, since damage occurs at the interface between the coating and substrate, and is also visible by optical microscopy if regions of the coating are removed.

2.4 LOW FLUX NEUTRON IRRADIATION UNDER INERT ATMOSPHERE

A total of 60 coupons and tube specimens with coatings prepared by ORNL and delivered to the Massachusetts Institute of Technology (MIT) Nuclear Reactor Laboratory (NRL) facility. These specimens were irradiated in the MIT NRL for approximately 66 days between July 18th and October 11th, 2016, accumulating an estimated fluence of 4.8×10^{24} n/m^2 (E > 0.1 MeV) between 280-340°C. Real time temperatures were monitored by thermocouples in axial locations within the capsule and typical variations were about ~3°C at full reactor power due to control of the He/Ne sweep gas in the capsules. Post-irradiation disassembly was conducted at the MIT NRL hot cell facility. Graphite holders were removed from the titanium capsule. The graphite holder with the

specimens is shown in Figure 3. The outer perimeter holds six chambers for coupons, while the inner core holes 4 cladding tubes.
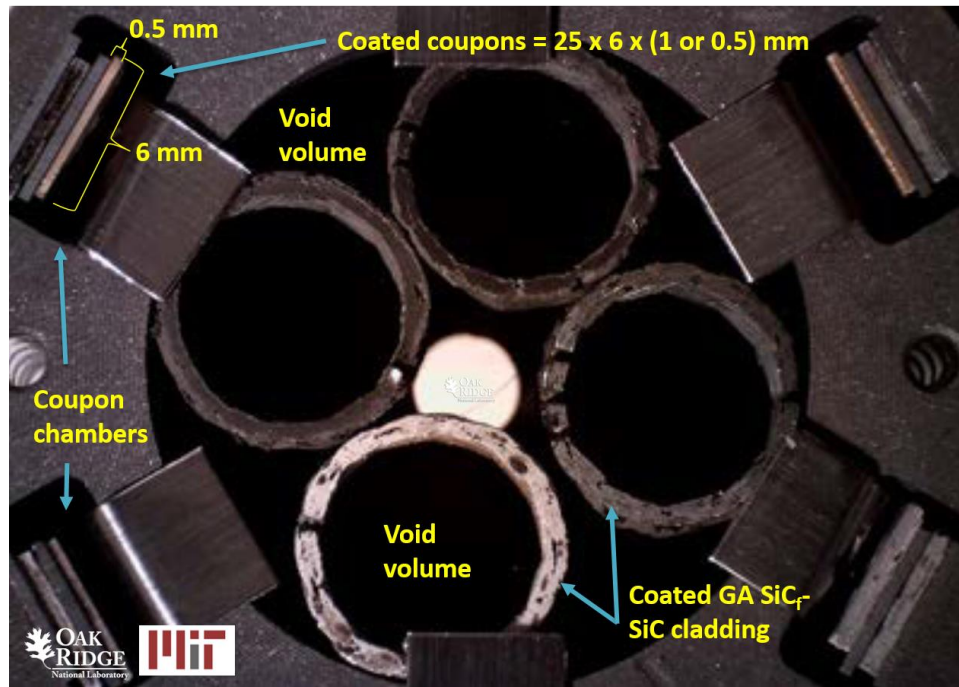
Figure 3. An image of a graphite holder (bottom-most capsule position) during disassembly. The radial rectangular coupon chambers and central void are shown; the central area holds the four composite tubes.

Specimens and shims (for smaller coupons) were unloaded from the six rectangular chambers at the circumference. Each chamber also held prototype coated cladding sections. No unusual issues were encountered during the disassembly process, and all specimens and shims appeared structurally-sound. Specimens, shims, flux wires, and springs were documented during the disassembly process and placed into numbered plastic vials. The dose rate of the total specimen collection (>5 R/hr at 10 cm as measured with the in-cell graphite matrix tube) precluded removing them from the cell in an unshielded container. Specimens were photographed from the Hot Cell prior to shipping.

2.5 AUTOCLAVE CORROSION TESTING UNDER SIMULATED BOILING WATER REACTOR CHEMISTRY

Initiation of autoclave hydrothermal corrosion testing was conducted after acquisition of post-irradiation data. Samples were focused more significantly on PVD coatings that were more promising than electrolytic or vacuum plasma spray due to early results from mechanical tests and radiation resistance. Substrates were 20 x 10 x 1 mm CVD SiC. Exposures were conducted using a controlled chemistry water loop simulating BWR normal water chemistry coolant in the

Hydrothermal Corrosion Laboratory (HCL) at Oak Ridge National Laboratory. A schematic of the water loop is shown in Figure 4. Samples were hung from zirconia rods in the 3.8 L Hastelloy 276 autoclave. A gas blend of 95/5 Ar/O$_2$ was bubbled through the main column to maintain a dissolved oxygen (D$_{O2}$) concentration of ~2 wppm.
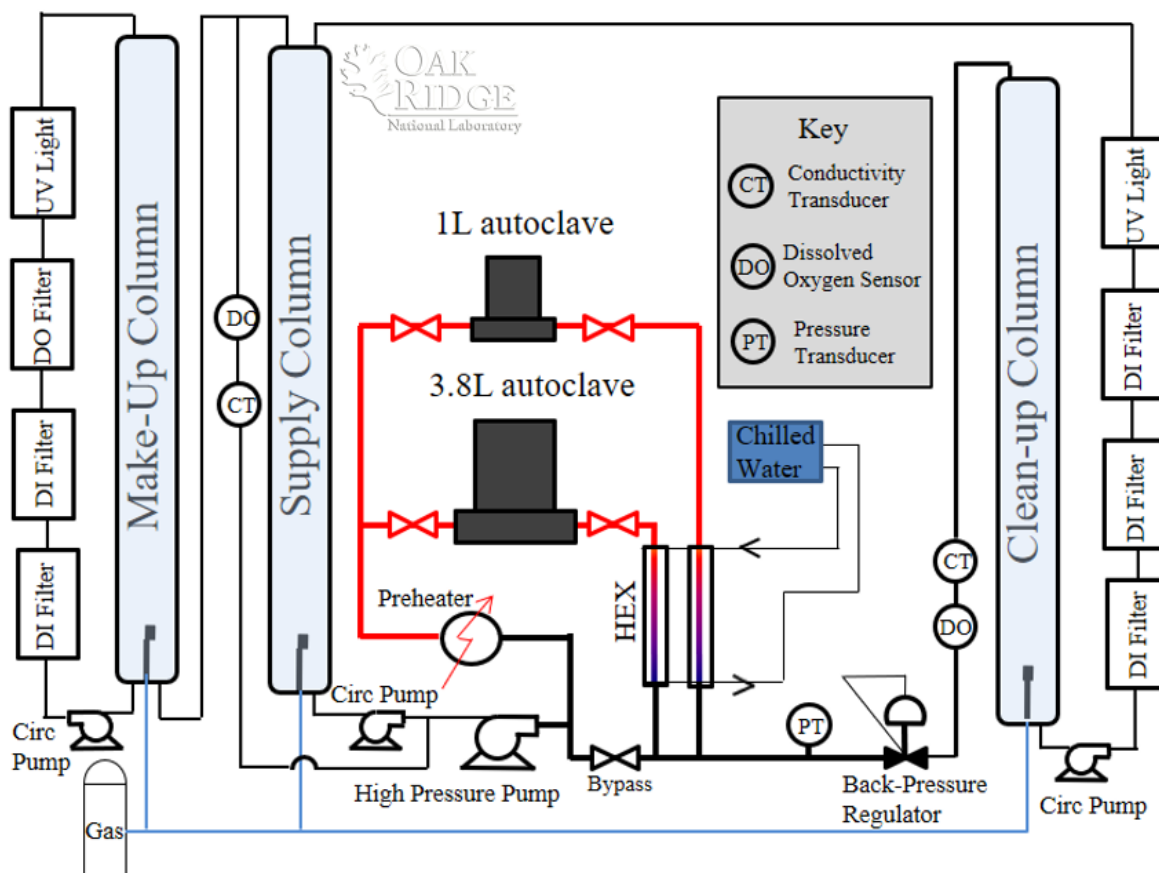
Figure 4. Schematic drawing of the controlled chemistry water loop at the hydrothermal corrosion laboratory at ORNL.

Water from the column was fed to a Pulsafeeder high-pressure pump, through a pre-heater, and into the 3.8 liter autoclave. The inner wall of the pressure vessel was comprised of Hastelloy 276, and the system was maintained at 288°C and 1900 psi. After exiting the autoclave, water was chilled and depressurized. Water then flowed into a clean-up column where it was collected and then run through a series of DI (De-Ionizing) filters and a UV (Ultraviolet) light before recirculating into the supply column.

2.6 PERMEATION TESTING STATION

A comprehensive ultra-high vacuum permeation testing station, established in the Low Activation Materials Development and Analysis Laboratory (LAMDA) at ORNL, was used to evaluate the hermeticity of the coated SiC_f-SiC composite tube. Figure 5 shows a schematic illustration of the permeation testing system.
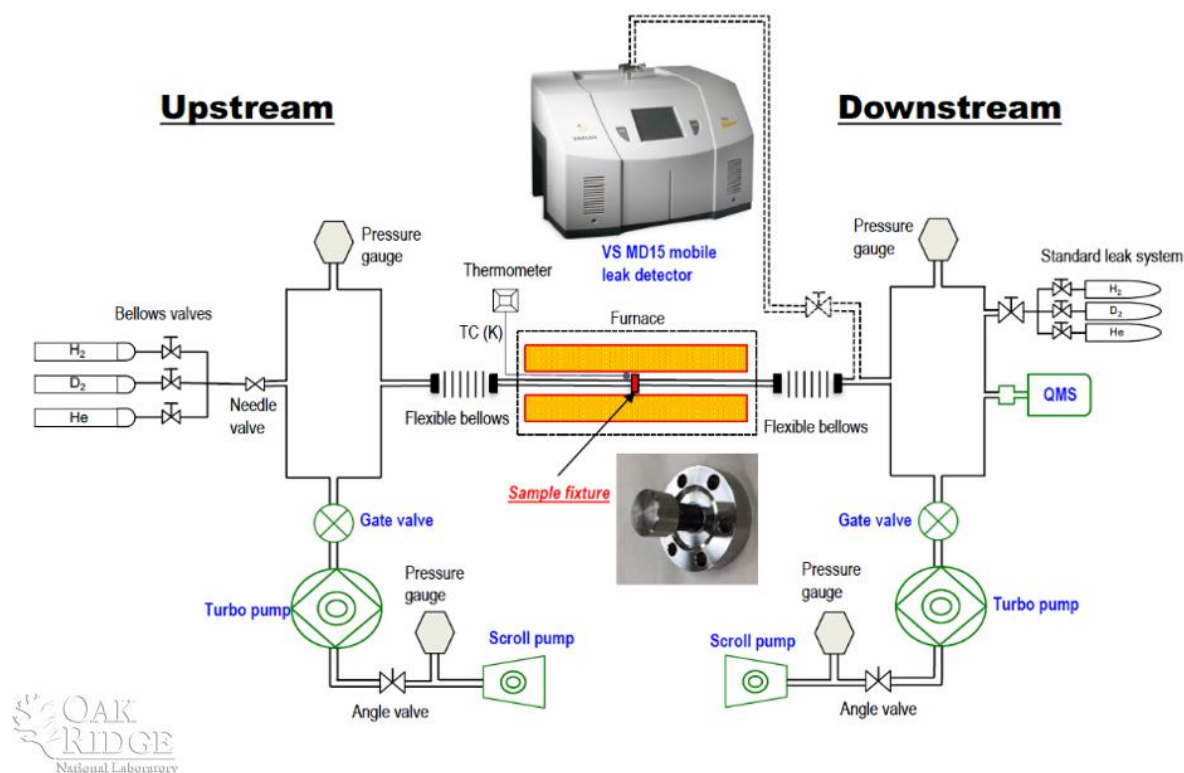
Figure 5. Schematic layout of the permeation test station.

The system consists of two major parts, i.e., the upstream section providing pressurized testing gas (i.e., helium and hydrogen isotopes) and the downstream section measuring the permeation gas. Epoxy was used to mount the coated SiC/SiC tubular samples to the substrate SS (stainless steel) flange and the SS cap. All testing was performed at room temperature to provide results on the hermeticity of the first-generation dual-purpose coating for SiC_f-SiC tubes. Further details of the system can be found in "M3FT-16OR020202114, ORNL-TM-2016-372 - Technique Development for Modulus, Microcracking, Hermeticity, and Coating Evaluation Capability for Characterization of SiC/SiC Tubes" while current results are being published in "M2FT-17OR020202102, ORNL-TM-2017 – Determination of He and D permeability of neutron-irradiated SiC tubes to examine the potential for release due to micro-cracking".

2.7 NEUTRONICS SIMULATION

The effect of increasing thickness of metallic coatings on fuel cladding was considered and modeled for neutron economy. Coatings which include Cr and Ti are of neutronic concern due to strong neutron absorption cross sections. Application of these materials in a nuclear reactor core would remove thermal neutrons otherwise available to induce fission, thereby imposing a neutronic penalty in terms of the achievable cycle length of the reactor and the associated fuel cycle economics. To assess this effect, computational models of typical LWR fuel assemblies are constructed for analysis with the SCALE6.1 code suite.[24] The T-DEPL sequence of the TRITON module is employed for this study to simulate depletion of individual fuel assemblies to a burnup of about 60 GWd/MT for cases of varying enrichment and coating thickness. Following these simulations, the linear reactivity model[25] is used to extend the single-assembly results to a typical 3-batch LWR core to glean a realistic estimate of the impact of assembly enrichment and coating thickness on cycle length. The 2D fuel assembly models are based on a Westinghouse 17x17 PWR, and the simulated operating conditions are selected to be representative of a PWR core environment. Table 3 details the fuel assembly geometry and operating conditions imposed on the SCALE models. [26-28]

Table 3. Fuel assembly geometry and operational conditions.[26-28]

Assembly Array	17x17
Guide Tubes per Assembly	25 (=24 control rods + 1 instrument
Specific Power	40 MW/MT
Fuel Temperature	900 K
Fuel Rod Pitch	1.26 cm
Fuel Pellet Radius	0.4096 cm
Fuel Clad Temperature	600 K
Fuel Clad Outer Radius	0.4750 cm
Fuel Clad Thickness	0.0572 cm
He Gap Temperature	600 K
Guide Tube Outer Radius	0.6121 cm
Guide Tube Thickness	0.0406 cm
Coolant Temperature	600 K
Coolant Density	0.70 g/cm3

The operational conditions such as clad and fuel pellet temperature distributions, and specific power were assumed based on typical PWR parameters and other similar fuel assembly depletion simulations in literature. Fuel enrichment was varied from 3% to 5%, and the metallic coating thickness, depending on the coating, was varied from 0 to 40 μm. The coating thicknesses were based on expected thicknesses noted in Table 2. Reflective boundary conditions are imposed on all fuel assembly models, thereby approximating infinite lattices. Table 4 details the case matrix for the study; in addition to the SiC assemblies, a case was run with Zircaloy-4 cladding of standard Westinghouse-type 17x17 PWR fuel assembly dimensions to provide a fundamental reference.

Table 4. Case matrix for Zircaloy-4/SiC cladding comparison with selected metallic coating.

Enrichment	Coatings
3-5%	Electrolytic Cr (0-30 μm) on PyC(0-10 μm) PVD CrN (0-10 μm) PVD TiN (0-10 μm)

Each fuel assembly model was depleted to about 60 GWd/MT, and the assembly reactivity was tracked at each burn step. Assembly discharge is assumed to occur when the reactivity reaches 0.03, accounting for an assumed neutron leakage of 3% that is not captured by the infinite lattice models.[26-28]

3. RESULTS

3.1 MICROSTRUCTURE OF ELECTROLYTIC CHROMIUM

The electrolytic Cr deposition was conducted by an external collaborator (NEO) using a proprietary hexavalent chromium bath. Dense electrodeposited chromium coatings typically experience over 1 GPa of tensile stress during densification while maintaining interface with the substrate.[29-33] If the interface is not maintained between SiC and the coating, this results in a sequence of tensile stress-derived failure matching the progression documented by Evans and Hutchinson.[34, 35]

Figure 6(a) shows surface preparation typical from grinding on 800-grit (25 μm) diamond, showing a surface roughness between peak and trough of about ~1-2 μm. Figure 6(b) shows a similar roughness caused by alkali and acid etching. All successful coupons with electrolytic Cr possess surface roughness discernable from the cross-section.
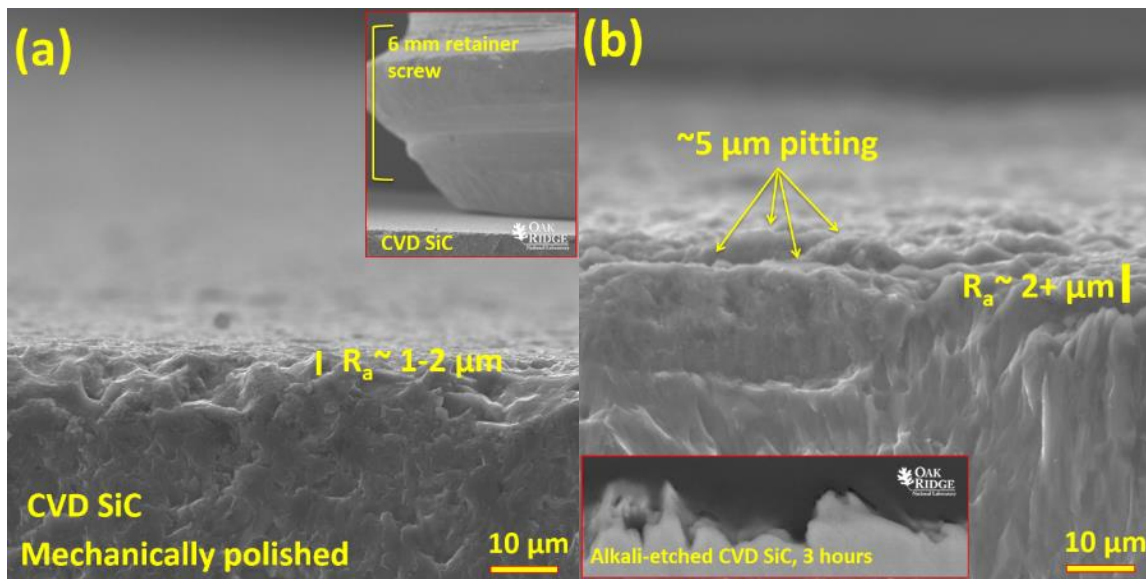
Figure 6. Surface roughening of CVD SiC mounted along the expected substrate interface, showing effect of (a) mechanical abrasion and (b) chemical etching. Etching produces a comparable morphology to mechanical abrasion.

The successful electrolytic Cr coating appeared to be well bonded when using a carbon bond coat based on pyrolytic carbon (PyC). PyC provides the electrical conductivity needed for electroplating. The coating technique is proprietary, but it appears that no significant change in electrolytic bath parameters is needed for deposition.

Figure 7(a) shows a cross-sectioned Cr coated PyC on SiC_f-SiC. It shows a 10 μm chromium layer applied on a 5 μm PyC layer. The PyC layer can be deposited on an etched overcoat, or can replace

the overcoat. This coating is referred to as SiC/PyC/Cr.
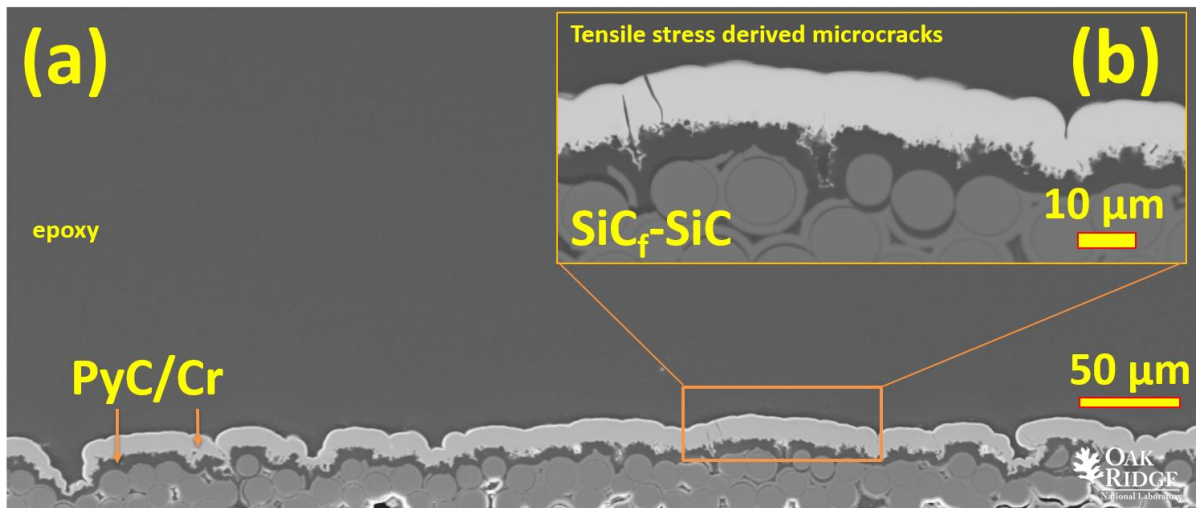
Figure 7. Cross-section of (a) SiC/PyC/Cr coating concept, while the inset in (b) shows an example of the tensile microcracks observed on the top coat.

Figure 7(b) draws attention to the types of local cracking damage for SiC/PyC/Cr material, showing the surface cracks in the top coat which may or may not penetrate into the substrate. The frequency of these cracks is typically 1:500 µm. The width of the cracks are consistent to the linear strain caused by tensile stress of the coating.[10]
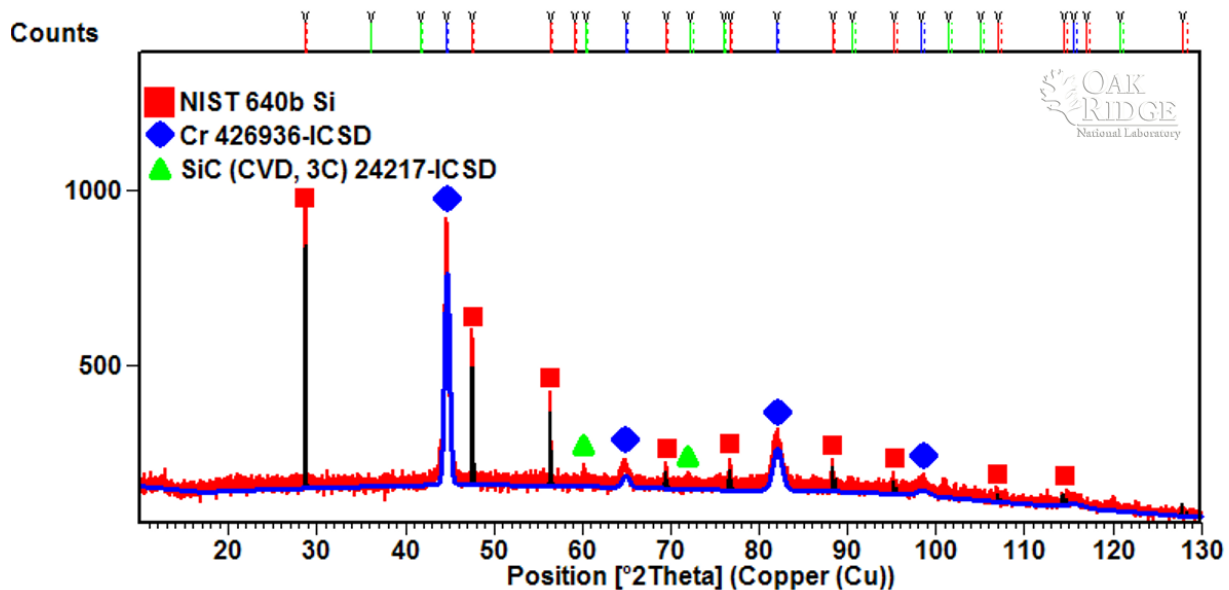
Figure 8. XRD pattern for SiC with 5 µm PyC and 10 µm electrolytic Cr (blue) deposit. Si (red) was used for specimen displacement and zero error calibration. A low intensity set of reflections (green) from the CVD SiC substrate can be observed.

Figure 8 shows the X-ray diffraction pattern for the SiC/PyC/Cr, complete with qualitative phase analysis. It shows the silicon internal standard and chromium present in the coating, with a small set of reflections indexing the substrate CVD SiC 3C polytype. The peak-width and angle-dependent strain broadening analysis from the Rietveld refinement showed the chromium annealed during deposition, and no microstrain was present in the coating.

In summary, the deposition of electrolytic chromium coating is possible on SiC when a suitable compatibility coat is used. However, the development of improved interfaces or interphases between SiC and PyC by integrated processing is limited. The current results will be published into a peer reviewed journal.

3.2 MICROSTRUCTURE OF CATHODIC ARC PHYSICAL VAPOR DEPOSITION

Materials coated using PVD were from two external vendors, Techmetals Inc, OH (referred to as TM) and Richter Precision, Inc, PA (referred to as RP). Proprietary coating parameters have not been disclosed but expected baseline process parameters are shown in Table 5.[36-40] The thickness, identified phases, lattice parameter, microstrain and crystallite size were derived from X-ray data and SEM cross-section. The multilayer CrN/Cr coating has two phases in the coating, and so two sets of derived data are shown.

Table 5. Overview of four PVD coatings, including expected process parameters and SEM/XRD derived data. Parenthesis indicates one derived standard error from specimen displacement.

Coating	TM-TiN	TM-CrN	RP-Cr	RP-Cr_xN_y-Cr multilayer	
Vendor	TM	TM	RP	RP	RP
Deposition Temperature(°C)	>350	>400	>400	>400	>400
Bias voltage (-V)	>10	>25	>50	>25/50	>25/50
Base pressure (Pa)	$<10^{-3}$	$<10^{-3}$	$<10^{-4}$	$<10^{-3}$	$<10^{-3}$
Thickness (µm)	<10	5-10	7	30/3	30/3
Lattice parameters (Å)	4.246(8)	4.177(9)	2.886(1)	CrN: 4.1765(5), Cr: 2.8948(5)	
Microstrain	0.251(82)	1.045(185)	0.097(7)	CrN: 0.232(17), Cr: 0.587(17)	
Derived crystallite size (nm)	202.5	61.7	Not available	181.1 and 126.1	

Figure 9 shows the morphology of the various coatings at the same magnification. All coatings were between 5-30 µm thickness. Figure 9(a)-(d) respectively shows the TM-TiN coating, TM-CrN, RP-Cr and a multilayer CrN/Cr coating.
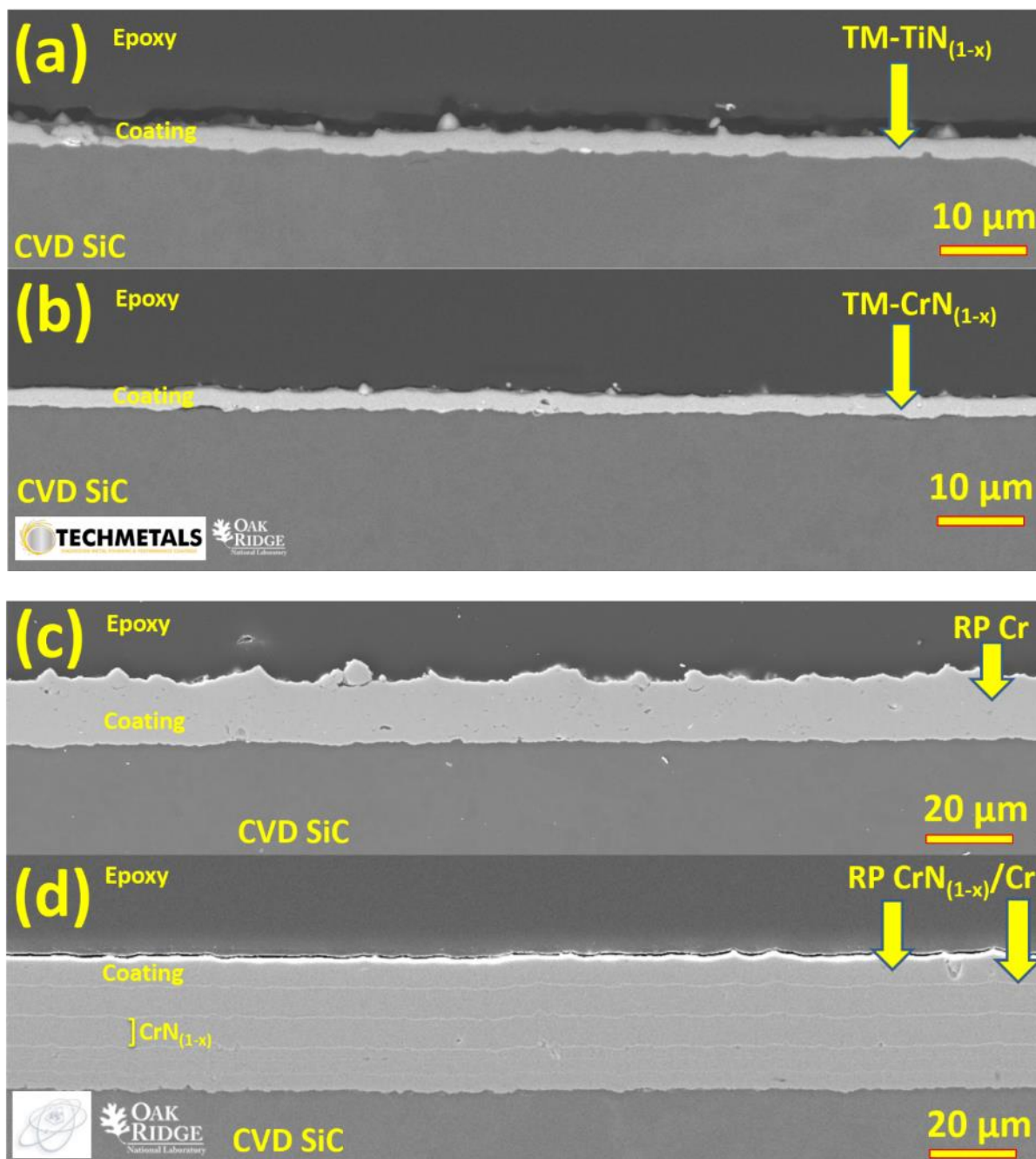
Figure 9. Backscattered electron SEM cross-section images of CVD SiC showing morphologies of (a) TM-TiN, (b) TM-CrN, (c) RP-Cr and (d) RP-CrN/Cr from PVD coating

The appearance of Physical Vapor Deposition by cathodic arc, even for identical compositions (e.g. Cr by electrolytic technique) is markedly obvious. For example, comparison of the two Cr coatings shows that PVD has no cracks and has a distribution of small gaps due to the "splat" morphology of evaporated metal impacting the surface at high velocity. The other feature of note

is that PVD coatings can be applied very thin, which is not feasible at present for the other coating technologies such as electrochemical plating and vacuum plasma spray.

3.3 MICROSTRUCTURE OF VACUUM PLASMA SPRAY

Deposition of Zr was conducted by external collaborator (Plasma Processes, LLC) using vacuum plasma spray (VPS). The metallic composition was Zircaloy-2. Previous reports indicated promising adhesion strength (by ASTM C633-01) and hermetic sealing[41] of VPS Zr, but challenges in the control of phases produced during deposition of zirconium. The first-generation coatings were deposited under DOE SBIR Phase I Grant No. DE-SC0011892.[42] Figure 10(a) shows the X-ray diffraction pattern from the first-generation coating. The qualitative analysis shows the presence of major phases ZrH_x and Zr from profile fitting overlay (blue) that matches the experimentally observed data (red).
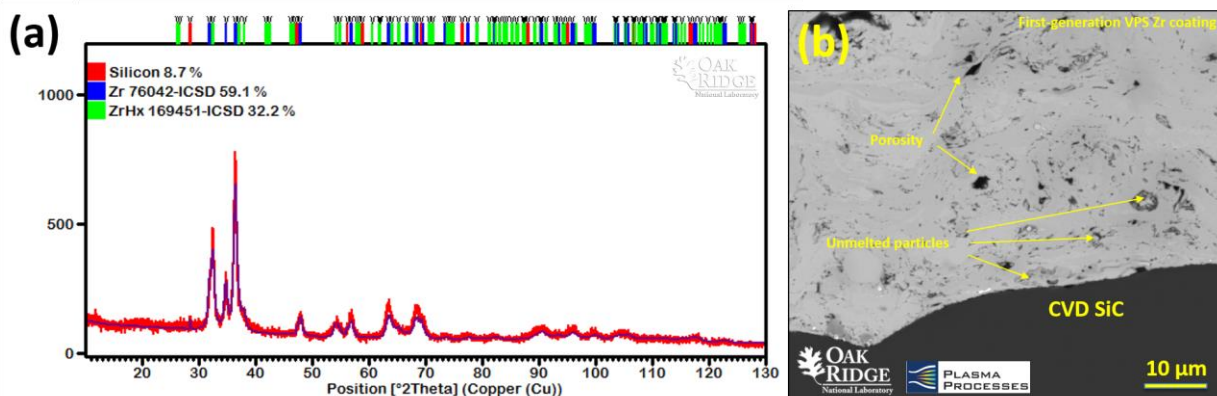
Figure 10. Analysis of first-generation VPS Zr coating by (a) XRD pattern showing the pattern fitting indicating presence of zirconium and zirconium hydride and (b) morphology of the coating in BSE mode, indicating varying contrast possibly caused by two phases, notable porosity and unmelted particles.

The microstructure of the VPS Zr on CVD SiC is shown in Figure 10(b), showing the typical thermal spray morphology, particularly porosity and powder particles. The morphology is derived from the metallic coating being in powder form and dispersed by a heated plasma gun by an inert carrier gas. The molten powder impacts the surface within a hot plasma, where it cools and solidifies quickly, resulting in a coating that may not be as dense as electrochemical or PVD coatings.

3.4 NEUTRONICS CALCULATION

Table 6 gives the single-batch discharge burnup interpolated from the reactivity trend as well as the 3-batch cycle length in effective full power days (EFPD) computed with the linear reactivity model. The case-wise combinations of coating thickness and enrichments were selected to efficiently isolate the impact of each variable. The effect of application of the absorptive coatings is readily apparent; nontrivial losses in cycle length due to the coating are seen in comparing cases

of matching enrichment. The average loss in cycle length due to application of 30 μm of electrolytic Cr is 11.9 EFPD; the penalty is dampened in cases with greater enrichment. It is also noteworthy that the PyC layer provides a slight boon to neutronics due to a small amount of additional neutron moderation, as observed in the cases with enrichment below 5% without the Cr layer. The neutronic penalty of Cr is ameliorated in switching to the CrN coating, which is applied in lesser thicknesses. Each of the CrN coatings analyzed reduced the cycle length by less than one week. The TiN coating is slightly less neutronically favorable than the CrN, with cycle length impacts on the order of one week. Additionally, a gain of 12.3 EFPD was achieved in replacing the Zr-based clad with SiC.

Table 6. Neutronic impact of the coatings on SiC

Coating	Enrichment	Single-Batch Discharge Burnup (GWd/MT)	3-Batch Cycle Length (EFPD)
None – Zr cladding reference	4%	30.78	384.8
None – SiC cladding	3%	22.92	286.5
None – SiC cladding	4%	31.76	397.1
None – SiC cladding	5%	40.09	501.2
10 μm PyC; no Cr	3%	22.93	286.6
10 μm PyC; 30 μm Cr	3%	21.96	274.5
5 μm PyC; no Cr	4%	31.80	397.4
5 μm PyC; 30 μm Cr	4%	30.83	385.4
10 μm PyC; no Cr	5%	40.09	501.2
10 μm PyC; 30 μm Cr	5%	39.17	489.6
10 μm CrN	3%	22.59	282.4
5 μm CrN	4%	31.53	394.2
10 μm CrN	5%	39.79	497.3
10 μm TiN	3%	22.44	280.5
5 μm TiN	4%	31.42	392.8
10 μm TiN	5%	39.66	495.7

The results of Table 6 are generalized by applying least squares regression to parameterize the computed 3-batch cycle length in terms of enrichment and coating thickness using the data from the cases with SiC cladding. End-of-cycle burnup, and therefore also cycle length, is assumed to be linear with respect to enrichment as well as the neutron multiplication of the coated assemblies. Perturbation theory[43] suggests that the assembly neutron multiplication varies with the reciprocal of the change in total absorption rate introduced by the coatings. This change in the total absorption rate is proportional to the volume of coating introduced. For the CrN and TiN coatings, the parameterization therefore takes the following form:

$$\hat{T}^{-1} = a\text{-}_0 + a_1 e^{-1} + a_2 t + a_3 t^2 \qquad (1a)$$

where T is the 3-batch cycle length (and the hat notation indicates the regression estimate), e is enrichment in percent, t is the coating thickness in µm, and the a_i's are the parameters. For the electrolytic Cr cases, it is desired to capture the effect of the PyC layer as well, yielding the following parameterization:

$$\hat{T}^{-1} = a_0 + a_1 e^{-1} + a_2 t_1 + a_3 t_1^2 + a_4 t_2 + a_5 t_2^2 + a_6 t_1 t_2 \qquad (1b)$$

where the subscripts 1 and 2 respectively refer to the individual PyC and Cr layers.

Carrying out the standard regression analysis [44] yields the following parameter values for the electrolytic Cr coating:

$$
\begin{aligned}
a_0 &= -3.312 \times 10^{-4} \\
a_1 &= 0.01149 \\
a_2 &= -1.073 \times 10^{-5} \\
a_3 &= 1.176 \times 10^{-6} \\
a_4 &= 2.089 \times 10^{-9} \\
a_5 &= 6.262 \times 10^{-8} \\
a_6 &= 1.484 \times 10^{-7}
\end{aligned}
\qquad (2a)
$$

For the CrN case, the parameters corresponding to Equation 1a are:

$$
\begin{aligned}
a_0 &= -2.979 \times 10^{-4} \\
a_1 &= 0.01136 \\
a_2 &= -6.404 \times 10^{-6} \\
a_3 &= 1.086 \times 10^{-6}
\end{aligned}
\qquad (2b)
$$

Finally, for the TiN case, the parameters are:

$$
\begin{aligned}
a_0 &= -3.184 \times 10^{-4} \\
a_1 &= 0.01144 \\
a_2 &= -3.764 \times 10^{-6} \\
a_3 &= 9.741 \times 10^{-7}
\end{aligned}
\qquad (2c)
$$

The increase in enrichment required to offset the introduction of a given coating thickness for maintenance of cycle length can be found by setting $e \rightarrow e + \delta_e$ and forcing the δ_e term to balance the coating thickness terms in Equations 1a and 1b. Rearranging the terms yields the following for electrolytic Cr:

$$\delta_e = \frac{\dfrac{e^2}{a_1}(a_2 t_1 + a_3 t_1^2 + a_4 t_2 + a_5 t_2^2 + a_6 t_1 t_2)}{1 - \dfrac{e}{a_1}(a_2 t_1 + a_3 t_1^2 + a_4 t_2 + a_5 t_2^2 + a_6 t_1 t_2)} \qquad (3a)$$

For CrN and TiN, the required additional enrichment takes the following form:

$$\delta_e = \frac{\frac{e^2}{a_1}(a_2 t + a_3 t^2)}{1 - \frac{e}{a_1}(a_2 t + a_3 t^2)} \tag{3b}$$

To assess these enrichment penalties for typical PWR assemblies, Figure 11 plots the increase in enrichment required to maintain cycle length as determined from Equations 3a and 3b for each coating as a function of the coating thickness over the range of thicknesses evaluated. The assembly enrichment is fixed at 4%, assumed to be a suitable average enrichment for a typical PWR fuel assembly. For the electrolytic Cr case, the PyC layer is assumed fixed at 10 μm.
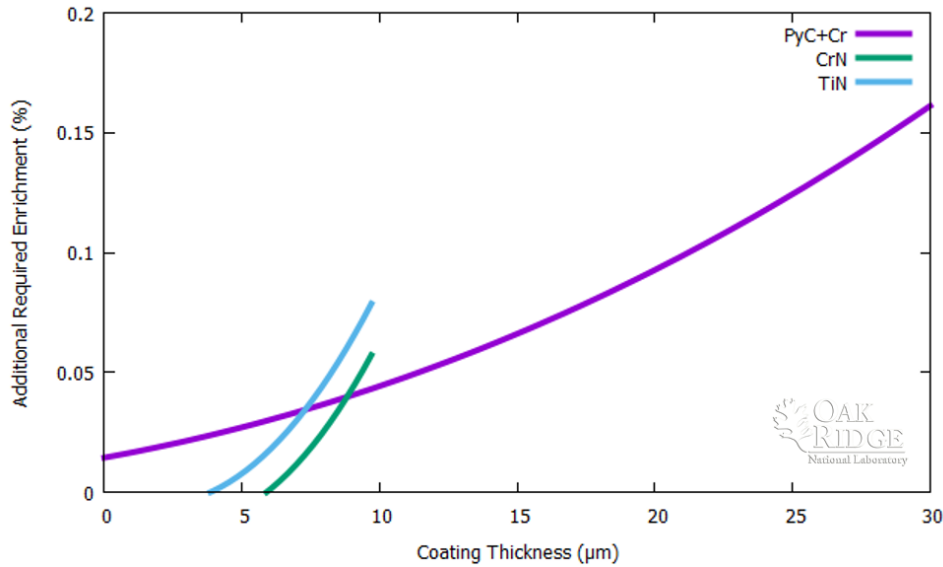
Figure 11. Increase in assembly enrichment required to offset coating reactivity penalty

Figure 11 reflects some interesting reactor physics effects regarding the behavior of each coating with increasing thickness. The electrolytic Cr carries the greatest effective absorption cross section of the coatings explored. The case of Ni/Cr previously published indicated significant neutronic penalties, cause by the thickness of Ni needed to maintain structural integrity of the coating.[10] However, the PyC layer from PyC/Cr case provides a moderative boon and the assembly reactivity is less sensitive to its thickness. Thus, beyond a certain coating thickness, the enrichment penalty of the CrN and TiN coatings exceeds that of the electrolytic Cr (~8 μm for CrN and ~7 μm for TiN). In any case, for the ranges of coating thickness considered, the additional enrichment required to maintain cycle length is modest; the greatest enrichment penalty found in the thickest electrolytic Cr case is well within 0.2% assuming PyC as the bond coat. Thus the economic impact is expected to be manageable, and therefore the PVD and VPS methods explored appear feasible[45] for commercial application.

3.5 MECHANICAL PROPERTIES OF COATED CVD COUPONS

The mechanical properties at the interface of the substrate and coating was investigated by debonding (by ASTM D4541) and scratch indentation (by ASTM E2546) tests. ASTM E2546 was only conducted on coated CVD SiC coupons, because the surface topology of SiC_f-SiC is typically not flat. The pre-irradiation test results are presented here.

The unirradiated interface debonding strengths are shown in Table 7, with epoxy reference strengths shown first, followed by the coatings. The epoxy reference samples were constructed by connecting two pull stubs with epoxy and removing them from one another. Table 7 shows that the epoxy strength is 22.0 MPa for 10 mm size pull-stubs. The test area was miniaturized for 5 mm diameter for irradiation coupons. When reference tests were conducted for comparison, no significant change in strength occurred, but the standard deviation increased by a factor of two. This indicated a less reliable moment of fracture and potential edge effects.

Table 7. Apparent debonding strength by ASTM D4541 tests of electrolytic chromium, vacuum plasma spray (Standard/first-generation) and PVD RP-CrN, RP-Cr, TM-CrN and TM-TiN. The interface strength could not be determined on the PVD samples

Substrate	Interphase	Main coating phase	Test diameter (mm)	Debond strength (MPa)	One stanard deviation(MPa)
Epoxy reference	-	-	10	22.0	6.5
Epoxy reference	-	-	5	23.3	12.1
VPS Zr	ZrC, Zr_5Si_4	Zr	5	17.3	14.5
SiC_f-SiC (unmachined)	PyC	Cr	5	3.6	1.4
SiC_f-SiC (machined)	PyC	Cr	5	5.9	0.8
CVD SiC (etched)	PyC	Cr	5	5.8	0.9
CVD SiC PVD RP-CrN	-	CrN/Cr_2N	10	>8.3	
CVD SiC and SiC_f-SiC	-	CrN/Cr_2N	5	Coupons failed	
PVD RP-Cr	-	Cr	10	>8.3	
CVD SiC and SiC_f-SiC	-	Cr	5	Coupons failed	
PVD TM-CrN	-	CrN	10	>8.3	
CVD SiC and SiC_f-SiC	-	CrN	5	Coupons failed	
PVD TM-TiN	-	TiN	10	>8.3	
CVD SiC and SiC_f-SiC	-	TiN	5	Coupons failed	

The VPS Zr debonding tests were conducted using the 5 mm pull stub configuration using a population of 18 tests, with a maximum debonding strength of 42.3 MPa. The average strength was 17.3 MPa. Results were consistent with a prior tensile test complying with ASTM C633-01 and values of 19-54 MPa were reported from a set of 5 tests.[41]

The data spread for VPS Zr did not include the debonding tests where interface failure occurred between pull stub and epoxy, and epoxy and coating, indicating that the debonding strength was high enough to reach the limit of the ability of the epoxy-stub system to remove the coating. This is a clear limitation of the test for assessing more robust, high strength coatings. Therefore, this population includes several test results where the epoxy did not remove the coating, and the strength must be cited for that test as the minimum epoxy strength value of >8.3 MPa.

In the SiC/PyC/Cr coatings, Table 2 shows that etching or machining apparently improved the adhesion strength of the coating, from 3.6 MPa to 5.8-5.9±0.8 MPa on average. All debonded coatings failed at the SiC/PyC interface. In fact, only a single test resulted in failure at the epoxy-stub interface.

The strength of the PVD coatings was not able to be accessed due to debonding at the pull-stub interface with epoxy. This indicating a high strength between SiC and the coating, or high stiffness of the coating itself. Instead, the minimum value of the epoxy reference tests was included for the 10 mm size tests (i.e. debonding strength must be >8.3 MPa) The test was not able to be conducted on the smaller irradiation coupons due to fracture of the substrate well before epoxy strength was reached.

In summary, the debonding test by ASTM D4541 adapted for small irradiation coupons is relatively limited, since it cannot test coatings with high adhesion strength. This is defined as the strength between epoxy and pull-stub. Since there is an interphase between VPS and PVD coatings with SiC, these have a higher adhesion strength compared electrolytic methods.

Scratch indentation is a test accompanied by complex interactive phenomenon between applied force, indentor shape, size and debris effects.[46-51] Despite the lack of quantitative understanding, the test is certainly used extensively as a simple comparative test to determine quantitative wear resistance, scratch resistance or to optimize processing for hardness or modulus. In this particular case, it was used screen processed coatings, and gain data for metrics such as the applied force at which the interface between SiC and the coating failed. It may also be used to compare material responses to gouging during fuel bundle insertion.

An example of a result is shown in Figure 12 for electrolytic Cr on Ni applied to SiC as a bond coat (SiC/Ni/Cr). First, the normal force (blue) and friction force (purple) increase linearly as the indentor travels across the surface of the coating.
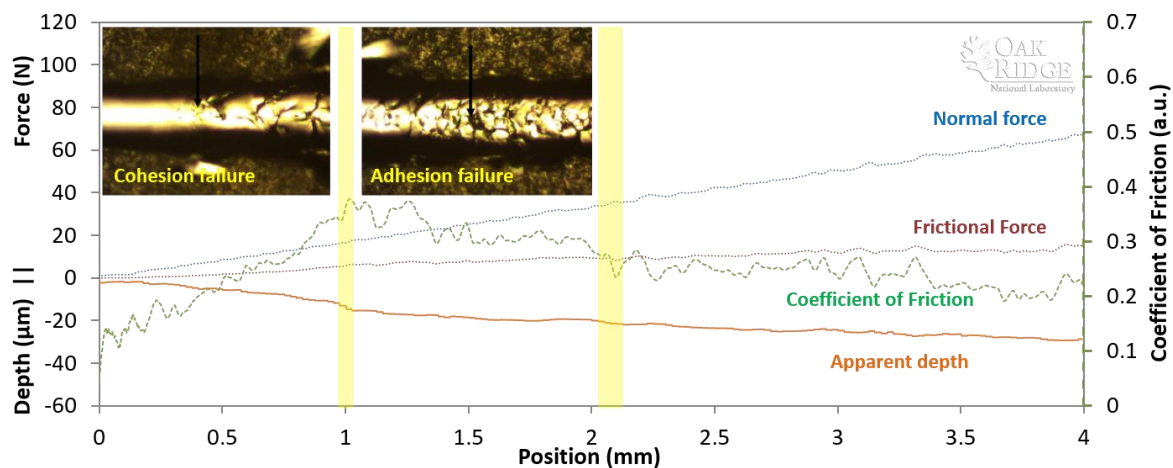
Figure 12. A coating of electrochemical Cr/Ni on SiC under scratch testing. This composition is used as an example to highlight pertinent features of the test. Two key regions, "Cohesion Failure" and "Adhesion Failure" are highlighted.

The data of interest is the "Coefficient of Friction" and "Apparent Depth". These two datastreams, coupled with microscopy (insets) determine the key load values of the test, which have been highlighted in Figure 12. Cohesion failure is typically found with the first crack in the coating, and is associated with the highest value in the coefficient of friction. A change in apparent depth is also observed, because the first crack-based deformation in the coating typically results in a penetration of the indentor into the flaw. Microscopy verifies the presence of a crack at this location. The second load of interest is known as adhesion failure, or coating removal. This is typically where the friction coefficient no longer increases and stabilizes, because the indentor is pressing the substrate while creating a wear track from the coating. The depth of the indentor can reach plateau as well. Values of load at "Cohesion Failure" and "Adhesion Failure" are plotted for all coatings assessed in this report. Cr (PVD and electrolytic) and PVD-TiN have high adhesion failure loads. In general, the PVD coatings perform well (the lower half (PVD RP Cr, TM-TiN, TM-CrN, RP-CrN and RP-CrN/Cr)) and are the most resistant to scratch-indentation by this test compared to VPS and electrolytic.
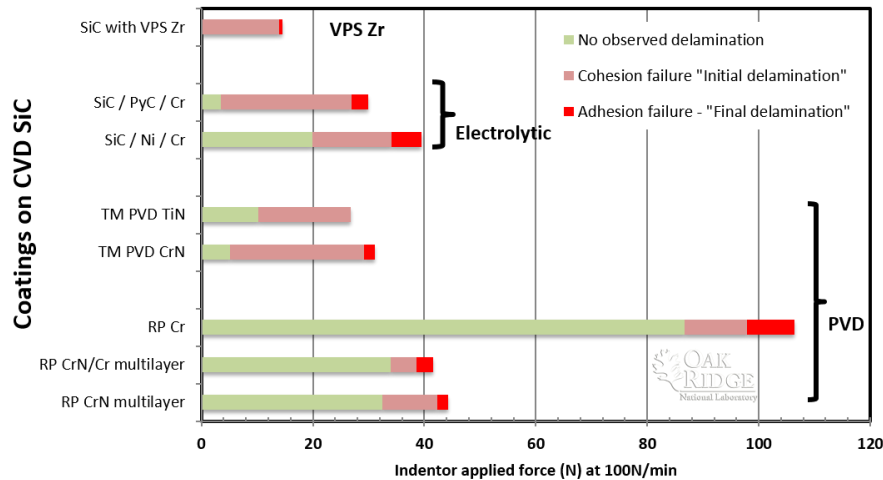
Figure 13.Failure phenomenon within scratch-indentation (by ASTM E2546) in all coatings as a function of applied force based on the two loads assigned to cohesion and adhesion failure.

The region before "Load at cohesion failure" is more of pertinent interest to coating performance, since this is defined as where the first sets of cracks are observed (microscopy) or detected (by depth change, rise in coefficient of friction or (if installed) acoustic emission). Unfortunately, the region before "Cohesion Failure", shown as green bars in Figure 13, is of limited understanding of phenomenon because the test cannot identify cannot identify whether the crack has occurred in the coating or substrate. To determine substrate-coating damage mechanisms, cross-sectioning was conducted. Figure 14 shows a series of cross-sections of the TM-CrN coating after the scratch test. These are focused-ion beam cross-sections of the coating at four locations corresponding to applied forces of ~0, 5, 10 and 15 N.

Figure 14 shows an evolution of substrate, coating and interface damage types as the force is increasing. The coating-substrate interface (a) initially has some cracks which extend into the coating. As the force increases, the coating also cracks (b) indicating cohesion failure. Spalling of the coating occurs as the force is increased (c) and (d), but delamination and removal of the coating is not observed.
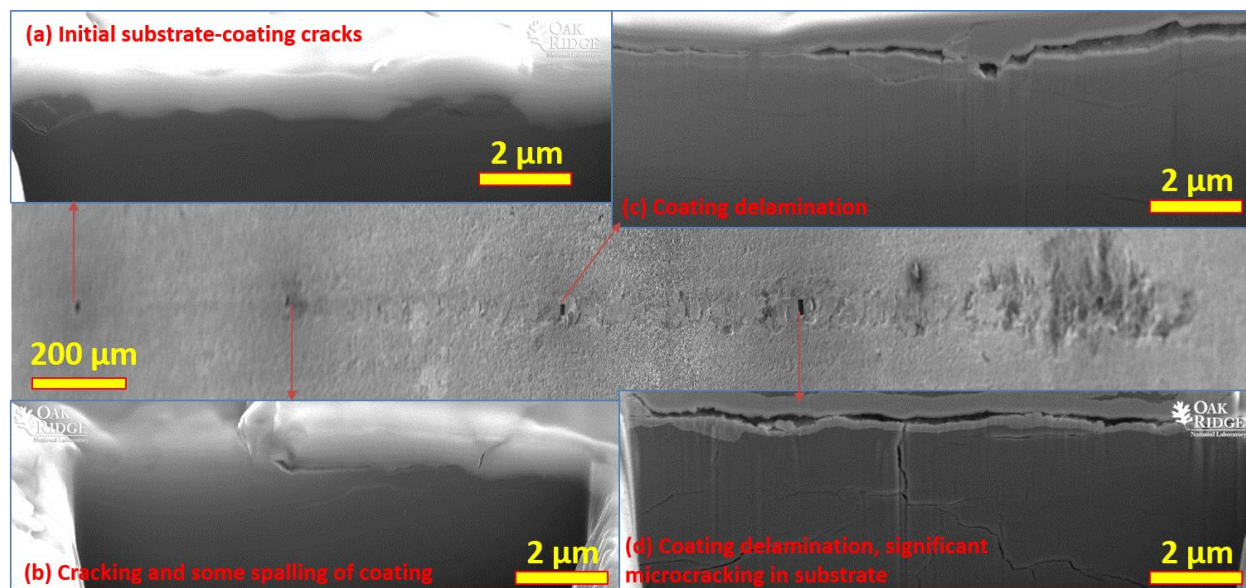
Figure 14. Actual phenomenon observed by cross-sectioning of coating TM-CrN corresponding to approximate indentor force at (a) 0 N, (b) ~5 N, (c) ~10 N and (d) ~15 N.

The SiC substrate shows cracking as early as Figure 14(b), which is expected given that these are ceramic-ceramic interfaces. The load values of the test for TM-CrN in Figure 13 do appear consistent with the evolution seen from the cross-sectioning. For example, based on Figure 13, cracks appeared to occur between 0 and 5 N applied force, and indicate the region of cohesion (coating) failure.

In summary, the debonding tests by ASTM D4541 are limited by epoxy strength, but can show that PVD coatings are more resistant to coating removal. The scratch indentation tests by ASTM E2546 show that PVD coatings are the most resistant to scratching due to higher loads at cohesion and adhesion failure. While the detection of cracks is possible by scratch-indentation, it cannot determine the location and type of damage without supporting cross-section analysis.

3.6 PERMEATION AND HERMETICITY

8 coated SiC$_f$-SiC tubes of duplex and triplex weave have been tested by using the permeation testing system. Initial evaluation of the hermeticity of tested samples was performed by using a mass spectrometer leak detector (VS MD15 from Agilent, Inc) to acquire the helium leak rate through the coated SiC/SiC tubes exposed to atmosphere. Table 8 shows the results for all tested samples.

Table 8. Helium leak rate of coated SiC/SiC tubes exposed in atmosphere at room temperature

Sample	Helium leak rate (atm-cc/sec)
No.1 TM-CrN	3.8×10^{-8}
No.2 TM-CrN	1.2×10^{-7}
No. 3 RP-CrN	$<1\times10^{-12}$
No. 4 RP-CrN	$<1\times10^{-12}$
No. 5 RP-Cr	2.9×10^{-10}
No. 6 RP-Cr	$<1\times10^{-12}$
No. 7 TM-TiN	$<1\times10^{-12}$
No. 8 TM-TiN	$<1\times10^{-12}$

5 out of 8 samples shows extremely low helium leak rate, indicating the gas tightness in atmosphere. TM-TiN and RP-CrN coated samples are all hermetic, while one RP-Cr coated sample is hermetic and the other is not. The TM-CrN coated samples are not impressive with respect to gas tightness based on this initial evaluation. However, the fraction of helium in air is only 5.2×10^{-6}, it is unknown whether these five 'hermetic' coated samples are still hermetic in pressurized gas environment. Of course, it is apparent that the No. 1, 2, and 5 will not have gas tightness at pressurized gas environments since large helium leak rates were already observed when exposed in air.

No. 3, 4, 6, 7, and 8 samples were further tested in pressurized helium and deuterium environment while the gas leak rates as a function of applied gas pressures were captured by using the quadrupole mass spectrometer in the permeation testing system. The testing results indicated that No. 3 PR-CrN, No. 6 RP-Cr, and No. 8 TM-TiN coated samples were hermetic in pure helium and deuterium environments with pressures up to 1.2 bar, manifested by the extremely low gas leak rate. In contrast, obvious gas leaking were observed in No. 4 RP-CrN and No. 7 TM-TiN coated samples at pressurized gas environment.

Figure 15 (a) and (b) shows the typical measurement data for a hermetic sample (No. 3 RP-CrN) and a non-hermetic sample (No. 4 RP-CrN), respectively.

(a)   No. 3 RP-CrN coated sample

(b)   No. 4 RP-CrN coated sample
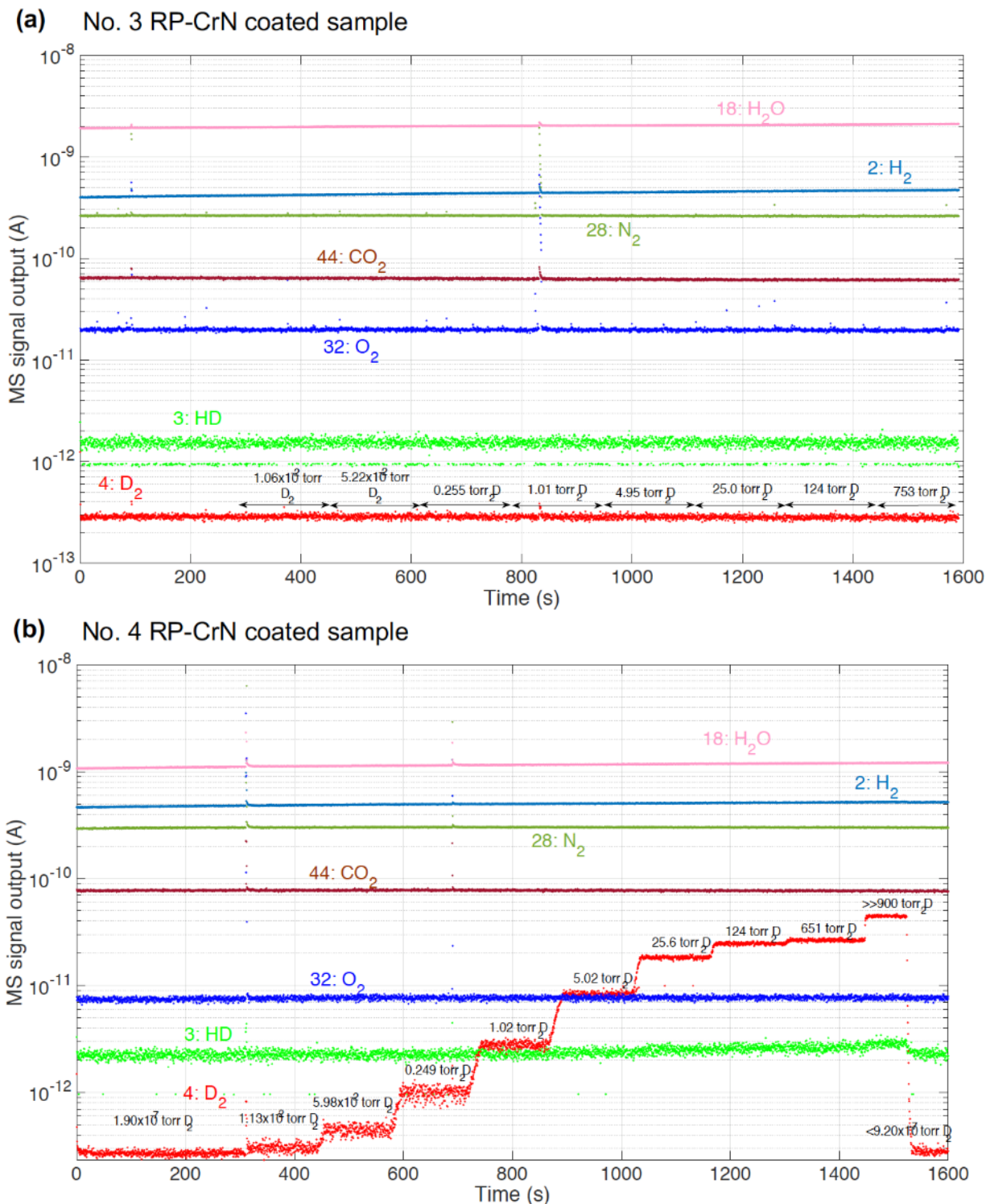
Figure 15. Mass spectrometer signals of gas elements captured in the downstream section of the permeation testing station of (a) No. 3 RP-CrN and (b) No. 4 RP-CrN coated samples as a function of deuterium pressure. The major remaining gas elements in the system were also given.

More details on the data analysis will be presented in "M2FT-17OR020202102, ORNL-TM-2017 – Determination of He and D permeability of neutron-irradiated SiC tubes to examine the potential for release due to micro-cracking". As one critical function of the dual-purpose coating layer on the SiC/SiC composite tubes, ensuring the gas tightness of the studied tubes has not been fully achieved in the first-generation coating method. The permeation testing indicated that even the samples using the same coating method have different performances. More efforts are needed to improve the coating qualities.

3.7 POST-IRRADIATION EXAMINATION

A selection of the post-irradiation results are shown rather than reporting an exhaustive list. The submitted coatings are summarized in Table 2. A combination of bond coats and coatings (topcoats) were developed. The irradiation include three bond coats (nickel silicide, zirconium silicides, and nickel) and seven top coat (PVD Cr, TiN, CrN, CrN/Cr, VPS Zr, Electrolytic Ni/Cr and PyC/Cr) compositions.

The electrolytic Cr entered the irradiation campaign with a Ni bond coat or PyC bond coat. Both entered the irradiation campaign with cracks present in the chromium layer based on consistent data from cross-sections indicating surface cracks in Cr and in some cases, penetrating the Ni or PyC layer. The cracks in Ni/Cr were previously reported in "M3FT-16OR020202113, ORNL-TM-2016-332 - Examination of Hybrid Metal Coatings for Mitigation of Fission Product Release and Corrosion Protection of LWR SiC/SiC" and cracks in PyC/Cr can be seen in Figure 7(b).

Figure 16 shows the surface of electrolytic Cr coatings after irradiation. The photography of the surface show that cracks became larger after irradiation. The peeling is the typical outcome of channeling cracking, particularly showing the delamination aspect of the tensile stress failure. Some coupon faces appeared to be unchanged.
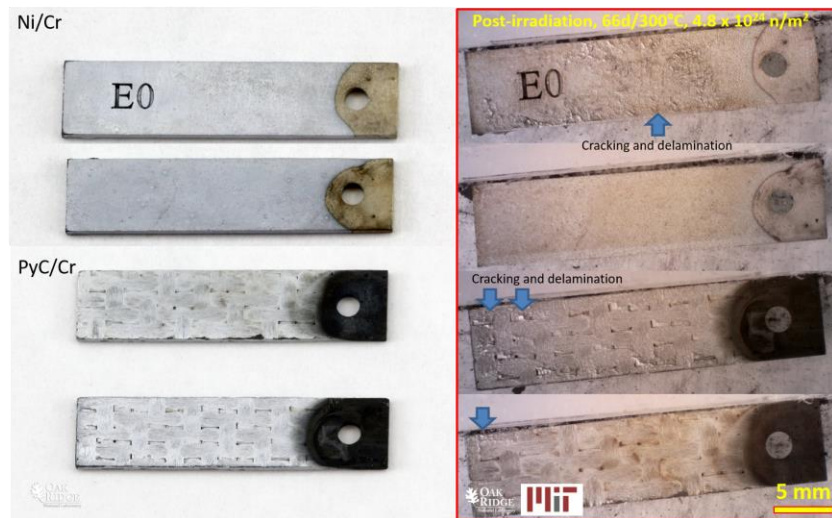
Figure 16. Optical microscopy of the surface of SiC/Ni/Cr and SiC/PyC/Cr coupons before and after irradiation.

The VPS Zr coatings entered the irradiation campaign with the phases of zirconium and its hydride on the surface of the SiC coupons. A small amount of zirconium silicide was detected on some of the coupons. Figure 17 shows the VPS Zr on coupons and tubes before and after irradiation.
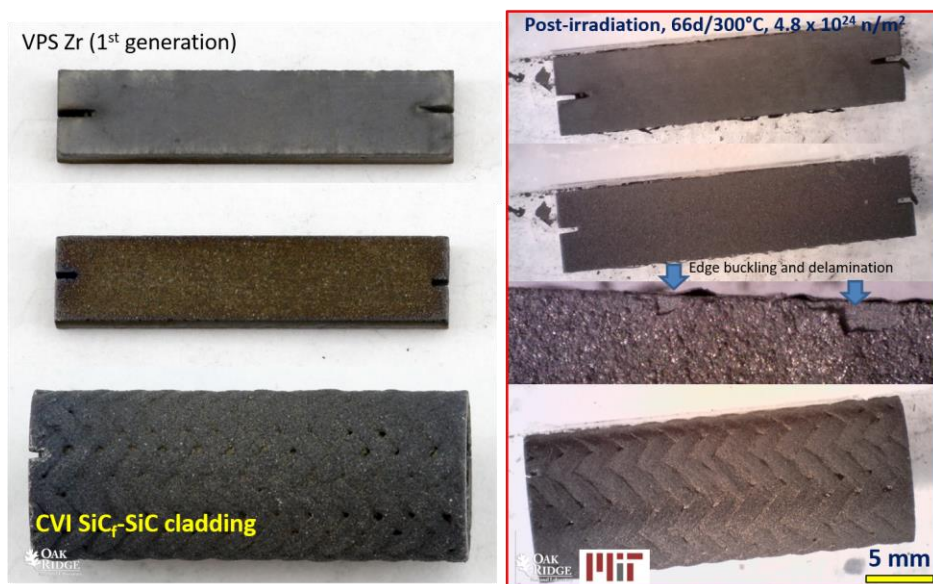
Figure 17. First generation VPS Zr coatings (bond coat) before and after irradiation, showing coupon edge with debonding, blistering and cracking. However, curved surfaces such as cladding showed no appearance of cracking.
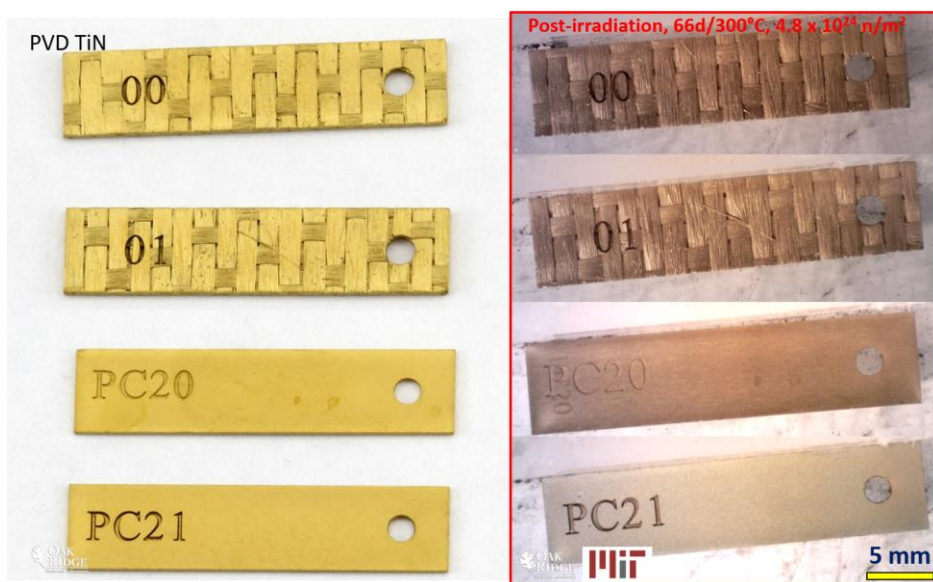
Figure 18. Examples of surfaces of PVD TiN showing absence of any damage on surfaces or edges. Discolorations were observed in high purity Cr (not shown) and the TiN (above) coatings.

After irradiation, the VPS Zr coating showed visible edge buckling and delamination (highlighted by the arrows in Figure 17), both in the higher magnification of the edges as well as pieces that have clearly fallen off into the plastic container. The coating on coupon faces and curvature of the cladding indicated no visible damage. This indicated that the vertexes may have increased stresses in the first-generation coating.

The PVD coatings from pre-irradiation characterization were typically crack free in the coating. Under optical microscopy, no cracking or peeling was found. Figure 18 shows the post-irradiation optical microscopy of PVD TM-TiN. There appears to be no interface or top coat peeling, cracking or debonding. A color change is observed, indicating that after irradiation, the TiN coating now reflects all visible light wavelengths. All the PVD coatings (not shown) either showed discoloration or color changes, but were otherwise unchanged from optical microscopy. In particular, no debonding or peeling was observed.

In summary, post-irradiation in inert atmosphere appeared to show increased damage in the coatings from neutron irradiation exposure for VPS and electrolytic coatings. The PVD coatings appeared to show only minor changes such as color differences.

3.8 AUTOCLAVE CORROSION TESTS

After exposure to reactor coolant in the absence of irradiation, samples were characterized using optical microscopy and SEM, and were weighed to determine mass change. Due to photographs after inert-gas reactor exposure that indicating PVD was the most promising (see Figure 18), the PVD RP-Cr, TM-CrN and TM-TiN were prioritized. An additional PVD composition of ZrN, was also included for evaluation. Three additional electrochemical coatings were included in the autoclave experiments – an electrochemical Ni coating that was used as a bond coat for PVD and electrolytic Cr, and an electrochemical NiCr (nichrome) alloy that was developed to reduce the tensile microcracking of high purity Cr. Unfortunately, no SiC/PyC/Cr coupons simulating the SiC/PyC concept were available for autoclave testing.

Figure 19 shows optical micrographs of the coated coupons before exposure, after 200 hours and 400 hours . Significant spallation of the Ni and NiCr coatings is visible in the sample, and it appears the majority was lost during the first 200 hour exposure. The PVD Cr coated coupon shows little sign of corrosion or spallation. The PVD CrN coating shows little sign of corrosive attack, although some spallation is visible near the edge. The PVD TiN and PVD ZrN coupons show significant signs of corrosive attack. These signs are the difference in surface color and finish between the center regions of the coupons and the edges.
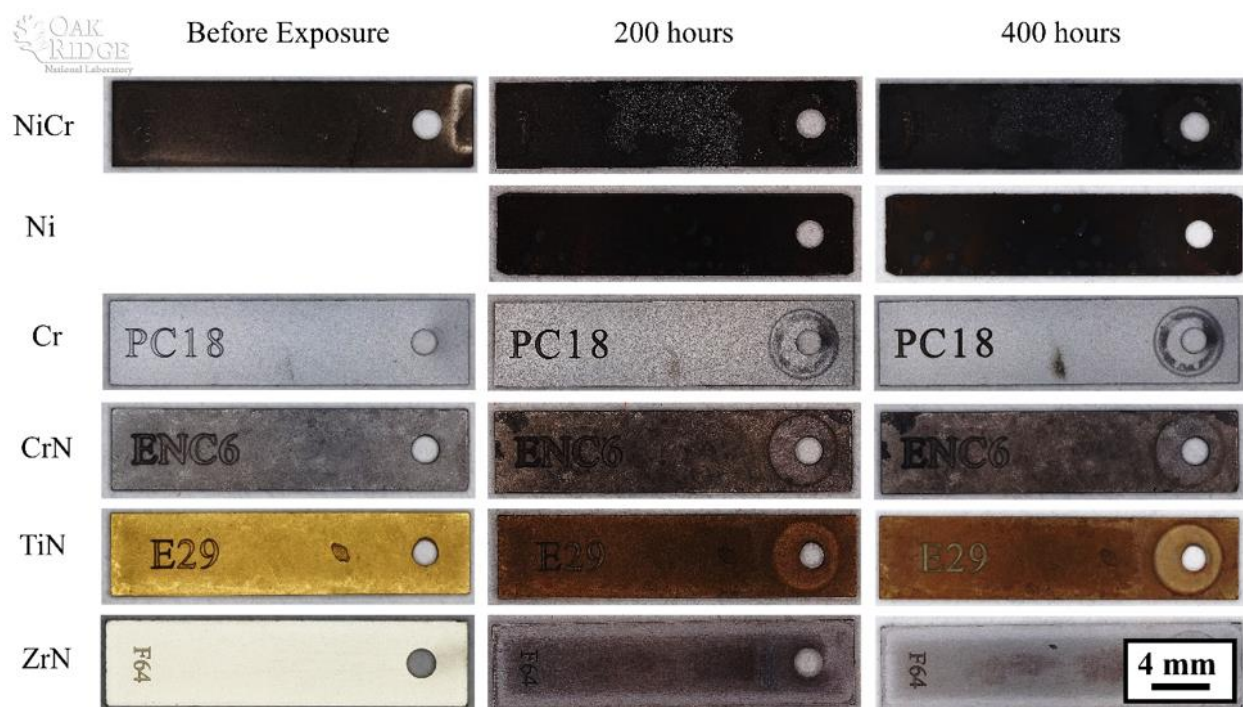
Figure 19. Light micrographs of coated coupons imaged before exposure, after 200 hours, and after 400 hours of exposure. Six different coupons are shown, each with a different coating applied to a SiC substrate. The Ni coated sample was not imaged prior to exposure.

Optical micrographs of the uncoated SiC, SiC_f-SiC, and solid coupons before exposure, after 200 hour of exposure, and after 400 hours of exposure are shown in Figure 20. Some signs of attack are visible on the SiC_f-SiC samples, but very change is visible on the uncoated SiC sample. The solid Cr and TiN samples show some signs of a surface oxide. The irregular shape of the TiN coupon is due to difficulty machining the material, since it was machined from a poorly densified TiN compact.

To measure mass change, samples were weighed before exposure, after 200 hours, and after 400 hours, and the results are shown in Figure 21. Both the solid TiN coupon and the TiN-coated coupon gained mass during the exposures, indicating the growth of an adherent oxide film, which is seen in Figures 18 and 19.

The SiC_f-SiC coupons both lost significant mass at a linear rate, while the uncoated CVD SiC sample lost a small amount of mass. Terrani et al. [6] reported a similar mass loss for a CVD-SiC sample exposed to NWC, but reported a mass *gain* for a sample of Hypertherm SiC_f-SiC during the first month of exposure, which disagrees with the mass loss observed after 400 hours in this work.
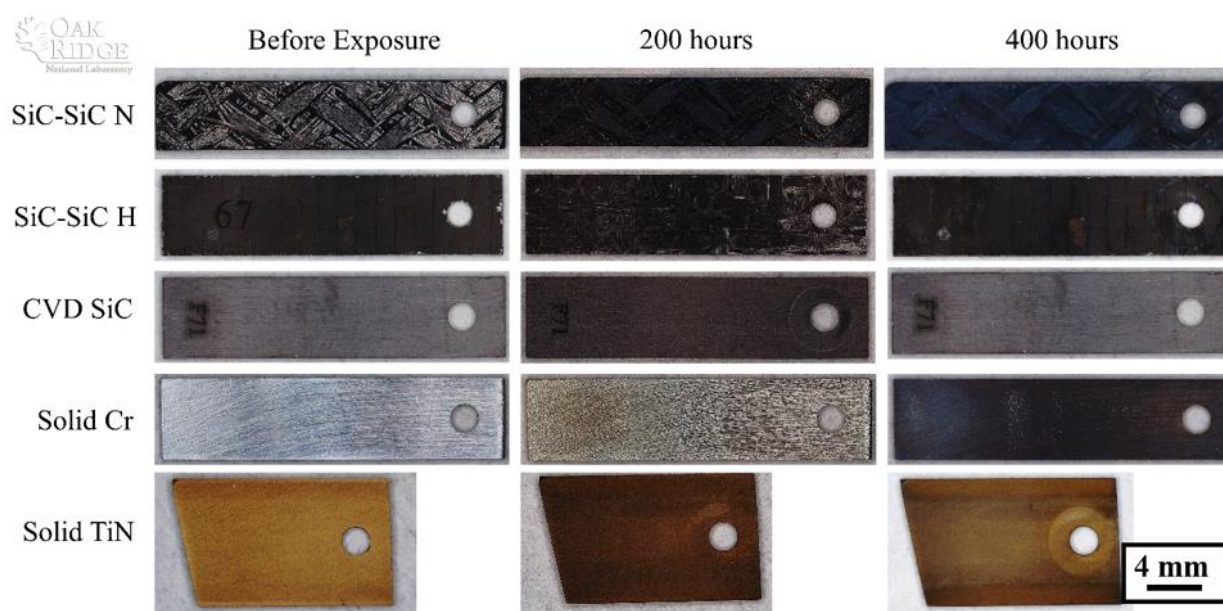
Figure 20. Light micrographs of uncoated SiC, SiCf-SiC, and solid coupons before exposure, after 200 hours, and after 400 hours of exposure. The irregular shape of the TiN coupon was due to difficulty machining the sample to the intended dimensions.

The solid Cr coupon and the Cr-coated coupon both lost mass at a relatively slow, and relatively linear rate. Due to the difficulty in casting pure Cr, the solid Cr coupon was very porous, and it can be reasonably assumed that this porosity accounts for the higher rate of mass loss seen in the solid Cr coupon compared to the Cr coated coupon.

The CrN coated sample lost mass at a higher rate during the first 200 hours exposure, and the rate of mass loss slowed during the second exposure. The spallation visible on the CrN coated coupon in Figure 19 is the likely reason for the higher rate of initial mass loss, and the slower rate of mass loss after 200 hours suggests that CrN may still be a viable mitigation coating. Edges of coupons represent stress concentrations due to the converging substrate-coating interfaces. The Ni coated sample gained a slight amount of weight, despite visible spallation of the coating.

NiCr and ZrN coated samples lost mass rapidly during the first 200 hours exposure, but the rate of mass loss slowed or stopped during the second exposure. The ZrN coupon's rapid weight loss appears to be the result of corrosive attack, as no spallation was visible on the sample. The rapid weight loss of the NiCr coupon during the initial 200 hours exposure, however, was likely due to large area from which the oxide spalled, as visible in Figure 19.
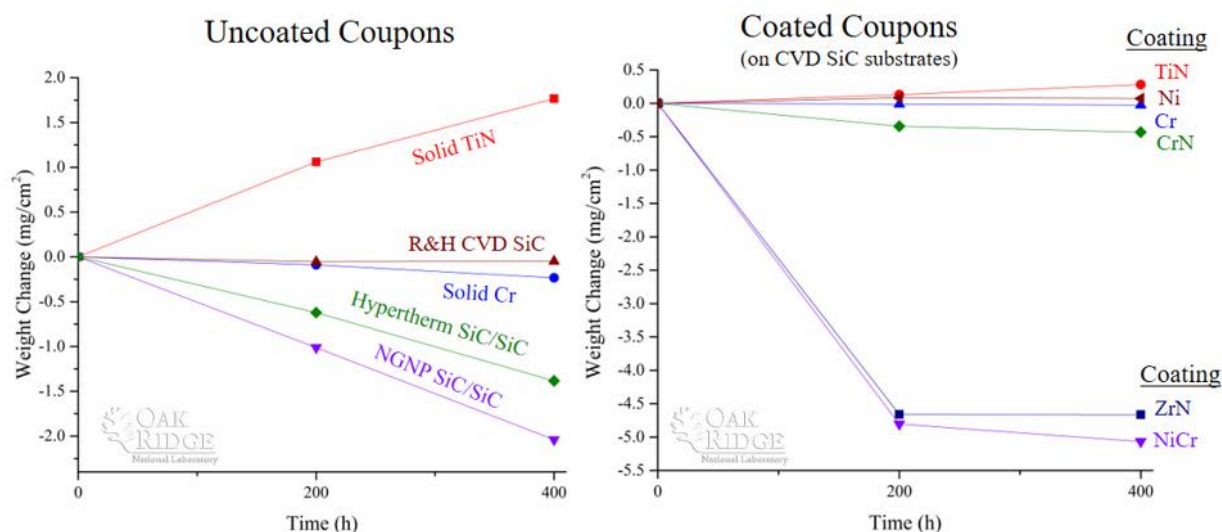
Figure 21. Mass change of uncoated and coated coupons. Values are graphed as the change in mass relative to the coupon mass before exposure.

The sample continued to lose mass during the second exposure, suggesting the coating is not a good candidate, even if it were to adhere to the substrate. The ZrN coupon did not lose moss during the second exposure, after a rapid mass loss during the first exposure. The images in Figure 19 do not show any spallation, so it is likely that the initial weight loss is due to corrosive attack, and the lack of weight change during the second exposure is possibly due to the growth of an adherent film concurrent with corrosive dissolution. Due to the rapid corrosive attack, ZrN is not a good candidate as a mitigation coating.

In summary, it appears that Cr and CrN are promising compositions if the coating can be deposited successfully on coupons; further, it appears that due to edge stresses, coupon geometries present much harsher test conditions than would otherwise be found on cladding where no sharp edges are present. TiN and ZrN appear to form oxides during exposure, but while TiN appears to have an adherent oxide, ZrN does not. The electrochemical NiCr coating does not appear to be a viable candidate unless further development is conducted.

4.   DISCUSSION

4.1 PROCESSING LIMITATIONS

While the criteria of hermeticity and corrosion resistance is clearly the key evaluator, the current available data clearly shows that composition and morphology from processing were the two dominant criteria for coating selection. Both VPS and electrolytic coatings represented development that could not solve these respective challenges.

First, the composition, particularly the top-coat (coolant facing), was a key determination for corrosion chemistry, and processing thus determined whether the coating was successful. The VPS

coating did not have the correct composition, and hermeticity/corrosion tests were not pursued apart from an initial trial. This trial revealed that the first-generation VPS Zr coating did not contain sufficient ground-state zirconium metal and furthermore, contained zirconium hydride. Figure 22 shows that under exposure to an autoclave (Westinghouse Electric Company, LLC) environment, the coating was removed. Apart from remaining regions of metal, the fiber architecture of th substrate clearly dominates this image. Furthermore, this is clearly more severe than the exposures coupons at 200 and 400 hours shown earlier with ZrN in Figure 19.
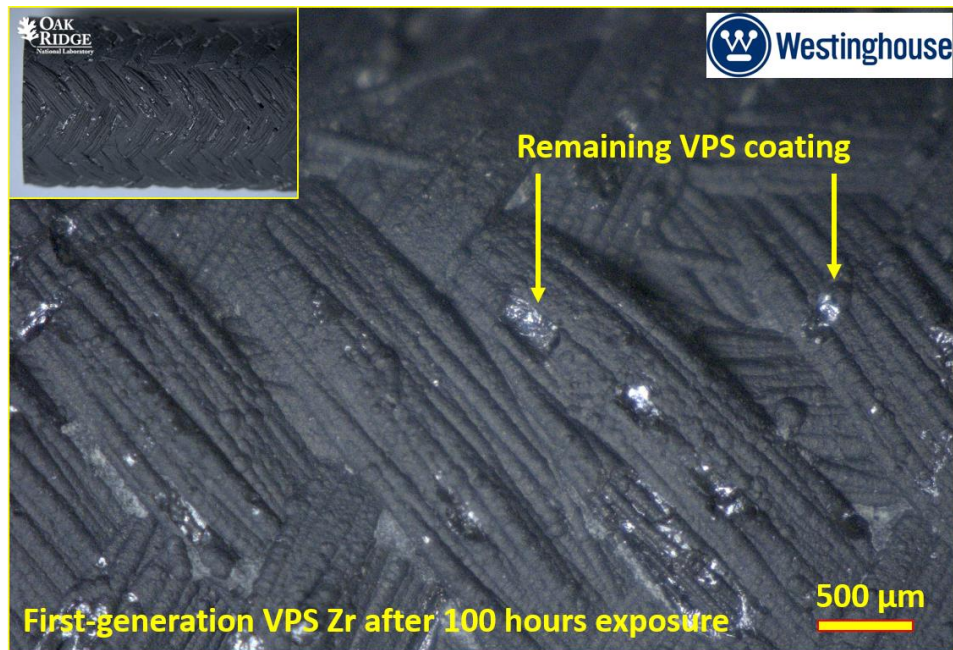
Figure 22. Photography of first-generation VPS Zr coating on SiC cladding after autoclave exposure for 100 hours. Only small amounts of the metallic coating has remained on the substrate.

Further autoclave tests were suspended until the VPS coatings were improved, and a processing-focused investigation was launched. The results from X-ray Diffraction and SEM cross-sections from two further optimizations are summarized in Table 9.

Table 9. Summary of effect of process variables of VPS Zircaloy-2 powder.

Processing Parameter	Effect of parameter change	Effect of the processing parameter on the coating quality
Gun stand off distance	Powder travel/velocity	Residual stress
Pre-heat of sample	Substrate temperature	Phases and bonding condition
Chamber pressure	Plasma flame envelope	Chemical reaction of plasma with metal powder

The outcomes of Table 9 included successful deposits with 75 wt% zirconium metal in the topcoat, with a small fraction of silicides and hydrides. However, all cross-sectioned samples with a high composition of Zr showed debonding at the interface between SiC and Zr. The delamination without substrate cracks was consistent with quenching stress [52-54] associated with the volume change of Zr[55] on cooling, which was higher than SiC volume change. This is typically controlled by reducing the temperature difference by solidifying to a higher pre-heat temperature. Unfortunately, a higher pre-heat temperature to mitigate quenching stress was associated with reduction in the zirconium content and led to higher hydride content. Further work is necessary to determine reaction kinetics of leading to hydride formation under the complex conditions and it is conceded that complete removal of the hydride phase is necessary for a viable coating. The results will be published in a peer-reviewed journal.

The second criteria for successful hermeticity/corrosion testing was morphology, which was also controlled by processing. Hermeticity and corrosion resistance are both sensitive to cracks in the coating, since a discontinuity of a topcoat interface cannot be a physical barrier. Morphology was a serious concern for electroplated chromium in both Ni and PyC bond coats. Microcracking (such as in Figure 7) associated with densification of Cr was the result of tensile stress relief agreeing with these results and prior literature.[29, 31, 32, 56] An initial surface crack expands and connects to other cracks, known as channeling. From here, the failure mode depends on values of interface toughness. If the energy required to break the interface is high, tensile cracks typically enter the substrate; if not, crack deflection and delamination occurs, leading to coating peeling from the interface.[34, 35, 57] If the cohesion of the coating is high, tensile stresses can also debond the coating without cracking. From the SiC/PyC/Cr coatings evaluated in detail here, the failure mechanism followed the classical tensile stress failure of coatings with weak interface. While channeling cracks could be mitigated by the Ni bond coat by electroless deposition, this was impractical, requiring ~30 μm bond coat to reduce tensile stress deflection of Cr. From neutronics calculations, such a thickness of Ni may be uneconomical (see "M3FT-16OR020202113, ORNL-TM-2016-332 - Examination of Hybrid Metal Coatings for Mitigation of Fission Product Release and Corrosion Protection of LWR SiC/SiC" for further details). However, interface engineering of PyC bond coat by CVD appears to be more promising in containing the tensile stress in high purity Cr than the previously developed Ni bond coats. Cracks appeared to penetrate the PyC layer in Figure 7(b) but appeared to be arrested. While this is promising, the interface of SiC/PyC could not be engineered further due to the absence of integrated SiC/PyC processing. At present, no CVD/I furnace is available for such a demonstration concept.

Table 10 summarizes the outcomes of the electrolytic coatings. SiC/Ni/Cr is possible but not feasible due to a need to apply ~60 μm of metallic bond coat and top coating resulting in a high neutron absorption cross-section. SiC/PyC/Cr is more feasible, but has yet to be demonstrated as an integrated process. This requires that during the final stage of composite infiltration, the PyC is reapplied, leading to a graded SiC-PyC interface on the surface of the cladding to improve the debonding strength. The weakness of PyC deposited on etched/cleaned CVD SiC is evident from the debonding tests. Secondly, a multilayer coating of chromium has not been demonstrated. Crack penetration depends on the stress concentration and tip geometry; cracks can also be deflected, channeled or mitigated by multiple layers.[33] A continuous interface is possible even with microcracking. Therefore, the preliminary concept of Cr/PyC on etched CVD SiC will be

published in a peer-reviewed journal, but is not ready for corrosion or hermeticity testing.

Table 10. Electrolytic Cr concepts attempted as mitigation coatings on SiC via two compatibility/bond coats.

Concept	Bond coat (μm)	Top coat (μm)	Interface	Remaining hurdles
PyC/Cr	10	>30	Potentially strong	SiC/PyC integrated processing
Ni/Cr	>30	>30	Very weak	Neutronic penalty

PVD coatings provided both correct composition and crack-free morphology, whereas electrolytic coatings were challenged by morphology (i.e. cracks) and VPS Zr coatings did not have the correct composition (i.e. zirconium metal in ground state). First, no cracking is observed in PVD coatings, due to the compressive stresses applied during the process. Cracks were preferentially observed in the SiC substrate or did not penetrate the coating. By controlling the bias voltage, the peening of evaporated metallic ions against the surface typically result in a compressive stress on the coating in the order of 1-20 GPa.[39, 58-60] This increases the stress required to force a crack open. The elevated temperature (~350°C) of PVD processing compared to electrolytic technique also encourages plastic deformation without cracking, since the ductile-brittle transition temperature of bcc α-Cr is cited as between ~50-80°C.[56, 61] Finally, no significant phase changes occur during PVD, whereas other coatings – such as VPS or electrolytic – currently appear to suffer major contributions from elimination of hydrogen, which typically shows volume shrinkage.[62] This demonstrates several advantages the PVD Cr possesses when compared to electrolytic Cr or current VPS development.

As a commercial process, there was intrinsic post-process stability. Neither electroplating nor VPS provided the latter, as their bond coats or interface design could not be optimized. Coating technology by its very nature is non-trivial. Briefly listed are some factors that must be considered during design[10]:

1. They are required to be thin, and yet often be part of supporting the same thermophysical challenges as the substrate, and the coating must accomplish its goal with very little bulk material.
2. They include intrinsic stresses from interface cohesion that defines a coating. Phase changes may also be intrinsic. Extrinsic stresses[16] (e.g. externally imposed by temperature) from coefficient of thermal expansion add an additional challenge, particularly for brittle materials.
3. A barrier coating cannot have non-uniformity and a single flaw is sufficient to define failure.
4. Barrier coatings require inventive strategy for long-term use, or else they are ablative, designed to recede and be reapplied. Successful coatings have typically used the environment to regenerate.

PVD coatings meet these design criteria since tensile stresses in the coating is the most likely failure mechanism of ceramic fuel cladding. The PVD coatings are intrinsically thin and can be modified with compressive forces to counter tensile stresses. Tensile stresses result in channeling cracks, whereas compressive stresses are beneficial in improving toughness. The elevated

processing temperature provides a higher mobility of atoms to rearrange during the process, which provides limited ductility. The last two requirements of the list require further development.

4.2 RADIATION STABILITY

The initial results indicated that first-generation coatings of PVD were more promising than their electrolytic and VPS counterparts. Both electrolytic and VPS coatings showed stresses in the coating that resulted in debonding. Under irradiation, the major stresses expected on the coating were tensile sign, due to a significant ~0.005 linear strain imposed by the swelling of SiC[63-65]. If interface cohesion is maintained, then the expanding substrate should force the coating into tensile stress. While metals typically expand at a greater rate per temperature increment than SiC, this was only expected to remove ~0.001 from the total strain[66]. The two unknown contributions to counter this tensile stress were swelling of the coating, radiation-induced creep, "instantaneous deformation" and microcracking. Since most coatings were brittle materials, the instantaneous deformation was likely limited to ~0.1-0.2%, after which microcracking should be observed. Therefore, swelling of the coating and radiation creep would be the critical contributions.

The failure of the first generation electrolytic Cr coatings appeared to follow the tensile stress sequence proposed by Evans and Hutchinson.[34, 35, 57] Surface cracks leading to channeling are not visible from optical microscopy, but peeling/delamination is seen in Figure 16. This indicated either tensile stress relief or increasing tensile stress probably led to cracks in Cr, PyC or Ni. The failure mode of the VPS coating on SiC appeared to show blistering. Blistering is typical of compressive stress in a coating, because the coating attempts to expand while maintaining the interface.[67]

The PVD coatings entered the irradiation campaign at a higher Technology Readiness Level since these were commercial products. Pre-irradiation examination confirmed coatings were mostly single phase, but textured with a high compressive stress. Compositions of these coatings had already completed successful in-pile exposures on Zircaloy-4 [12-14] indicating that the topcoat composition was compatible with reactor coolant and neutron irradiation. The optical microscopy observations showed that PVD coatings appear to be more promising due to absence of significant changes observed after irradiation. This is interesting because there is a significant tensile stress imposed on these coating compositions from swelling of SiC[63-65], and their phases – particularly with compressive stresses – are closer in mechanical behavior to brittle materials (bcc-Cr and metallic nitrides). The absence of catastrophic, optically observed failures suggests other mechanisms at work, such as substrate compression, radiation induced creep and swelling of the coating. Further work is planned to investigate these phenomena.

4.3 CORROSION RESISTANCE AND HERMETICITY

The results from the autoclave tests are generally consistent with expected literature. As previously noted, selection of the top-coat materials was based on their corrosion resistance in light water reactor coolant. The dominant developments were in processing techniques driven to make top coats compatible with SiC.

Currently, both Cr and CrN are reportedly suitable as coatings on Zircaloy-4, and are compatible with LWR coolant.[11, 13, 14] TiN is shown to be promising in LWR coolant in the absence of irradiation[15, 68], but it appears that TiAlN and CrAlN dissolve in-pile.[12] From the review of the materials thus far, hydrothermal corrosion resistance appears to favor a single phase oxide at the coolant-coating interface, a dielectric oxide that is also stable in the liquid medium, and adherent (strong chemical bond to substrate or low Bedworth-Pilling ratio, etc) to the substrate or topcoat. Obviously, any material deposited on the substrate cladding must also have sufficient adhesion and adequate morphology.

As previously emphasized, a failure in morphology – such as cracking – disqualified a coating from evaluation as it assumes that the coating no longer functions as a barrier. The drastic spalling and loss of the nichrome (NiCr) coating appeared to indicate that there were pre-existing cracks in the coating, which would be consistent with previous analysis of electrolytic coatings containing Cr. The corrosion results from Cr (from PVD) and Ni (electrochemically deposited) as phases appear to be consistent with literature[69-71], indicating their general stability in coolant. The results from autoclave tests showing uniform corrosion rather than spalling also support the absence of cracking in PVD Cr.[10, 22, 23] The results from Cr appear to be the most promising, since it indicated neither significant weight gain from oxygen or loss of the coating itself. The weight gain from Ni may be associated with uptake of oxygen to form a NiO.[71] However, Ni was included as a bond coat, rather than a top coat. In CrN, the results indicated a weight loss rate that decreases with exposure time, suggesting that there was dissolution of the oxide layer. The rate of mass loss appears to be in contradiction with previous results that showed no recession of the coating at all.[11, 12] Dissolution of the oxide layer or the coating material also appeared to occur in a uniform fashion with the PVD ZrN, indicating that it is not suitable for reactor coolant. Finally, TiN appears to be gaining weight due to uptake of oxygen. The TiN coated sample gained 0.28 mg/cm^2, which was greater than the mass gain of 0.02 mg/cm^2 reported by Elat at al for TiN coating on Zircaloy exposed for ~400h in 360°C water with <45 ppb DO.[15] The much lower DO content in Elat's exposure is the likely explanation for the slower oxidation rate.

The hermeticity results were only conducted on the PVD coatings, due to poor morphology of the electrolytic and VPS coatings. Early experimental details can be found in "M3FT-16OR020202114, ORNL-TM-2016-372 - Technique Development for Modulus, Microcracking, Hermeticity, and Coating Evaluation Capability for Characterization of SiC/SiC Tubes" while current results are being published in "M2FT-17OR020202102, ORNL-TM-2017 – Determination of He and D permeability of neutron-irradiated SiC tubes to examine the potential for release due to micro-cracking". The coatings are still first-generation commercial products without engineering for hermeticity. A future strategy is to attempt multilayer coatings (seen in CrN/Cr and TiN/TiAlN[15]) which might influence leak rates by increased diffusion path. At present, it appears that the coatings have potential but are not engineered for hermeticity.

5. SUMMARY

Evaluation has been completed on coatings based on their need to be a dual-purpose material for SiC. It is apparent that processing, which controls morphology and composition, played a key role in determining whether coatings could even be tested. Morphology challenges included cracks during processing and composition determined whether the coating was stable in reactor coolant. Both Vacuum Plasma Spray and Electrolytic technologies were immature and it was assumed that respective Zr and Cr-topcoats were not ready. All PVD coatings are potentially useful as dual-purpose coatings, due to superior morphology and microstructure. Table 11 shows a summary of the results of the evaluation:

Table 11. Summary of evaluation of first-generation coatings by corrosion resistance, hermeticity, compatibility with SiC interface under irradiation, and future research directions.

Coating technology	Phases in system	Coolant compatible	Hermetic sealing	Radiation compatible with SiC	Future research directions
Electrolytic	PyC/Cr	Unknown	Unknown	Potentially	Processing - Integrated SiC/PyC
VPS	Zr/ZrHx	No	Potentially	Unknown	Processing - Control of phases during spray
PVD	TM-CrN	Yes	Potentially	Yes	Composition and stress analysis needed
PVD	TM-TiN	No	Yes	Yes	Hydrothermal corrosion resistance
PVD	RP-CrN	Yes	Yes	Yes	In-pile hydrothermal corrosion
PVD	RP-Cr	Yes	Potentially	Yes	Hermeticity and in-pile corrosion

Table 11 shows that from the analysis of the PVD coatings, it appears that Cr is the most promising, as well as variants of CrN. However, there appears to be inconsistencies between recession and weight gain of CrN and TiN coatings that requires further data. Finally, in-pile irradiations of coatings under "Hybrid Coatings (HYCO) program" with coolant exposure are in progress at the Massachusetts Institute of Technology Nuclear Reactor Laboratory. Results from post-irradiation examination (PIE) will provide valuable insight into coating-SiC interface behavior. Discolorations in coatings after irradiation may also need investigation. Finally, second-generation coatings are being planned with industrial collaborators to optimize the microstructure depending on the results from hermeticity tests and PIE from HYCO irradiations.

6. ACKNOWLEDGEMENTS

7. REFERENCES

1. Zinkle, S.J., et al., *Accident tolerant fuels for LWRs: A perspective.* Journal of Nuclear Materials, 2014. **448**(1–3): p. 374-379.
2. Pint, B., et al., *Material Selection for Accident Tolerant Fuel Cladding.* 2014.
3. Khalifa, H.E., et al., *Fabrication and characterization of joined silicon carbide cylindrical components for nuclear applications.* Journal of Nuclear Materials, 2015. **457**: p. 227-240.
4. Stone, J.G., et al., *Stress analysis and probabilistic assessment of multi-layer SiC-based accident tolerant nuclear fuel cladding.* Journal of Nuclear Materials, 2015. **466**: p. 682-697.
5. Deck, C.P., et al., *Characterization of SiC–SiC composites for accident tolerant fuel cladding.* Journal of Nuclear Materials, 2015. **466**: p. 667-681.
6. Ben-Belgacem, M., et al., *Thermo-mechanical analysis of LWR SiC/SiC composite cladding.* Journal of Nuclear Materials, 2014. **447**(1–3): p. 125-142.
7. Barringer, E., et al., *Corrosion of CVD silicon carbide in 500 C supercritical water.* Journal of the American Ceramic Society, 2007. **90**(1): p. 315-318.
8. Hirayama, H., et al., *Corrosion behavior of silicon carbide in 290 C water.* Journal of the American Ceramic Society, 1989. **72**(11): p. 2049-2053.
9. Kim, W.-J., et al., *Corrosion behaviors of sintered and chemically vapor deposited silicon carbide ceramics in water at 360 C.* Journal of materials science letters, 2003. **22**(8): p. 581-584.
10. Ang, C.K., et al., *Examination of Hybrid Metal Coatings for Mitigation of Fission Product Release and Corrosion Protection of LWR SiC/SiC*. 2016, Oak Ridge National Laboratory (ORNL), Oak Ridge, TN (United States).
11. Van Nieuwenhove, R., et al. *Investigation of coatings, applied by PVD, for the corrosion Protection of materials in supercritical water*. in *6th International Symposium on Supercritical Water-Cooled Reactors, ISSCWR-6, Shenzhen, Guangdon, China, Mar*. 2013.
12. Van Nieuwenhove, R., et al., *In-pile testing of CrN, TiAlN and AlCrN coatings on zircaloy cladding in the Halden reactor*, in *STP1597 ASTM International's STP: Selected Technical Papers on 18th International Symposium on Zirconium in the Nuclear Industry*. 2017.
13. Brachet, J., et al., *Behavior under LOCA conditions of Enhanced Accident Tolerant Chromium Coated Zircaloy-4 Claddings*, in *Top Fuel 2016, Boise, ID, September 11-15, 2016*. 2016.
14. Brachet, J., et al., *On-going studies at CEA on chromium coated zirconium based nuclear fuel claddings for enhanced Accident Tolerant LWRs Fuel*, in *TopFuel 2015, (13-19 Sept. 2015), Zurich, Switzerland*. 2015.
15. Alat, E., et al., *Multilayer (TiN, TiAlN) ceramic coatings for nuclear fuel cladding.* Journal of Nuclear Materials, 2016. **478**: p. 236-244.
16. Spaepen, F., *Interfaces and stresses in thin films.* Acta Materialia, 2000. **48**(1): p. 31-42.
17. Sahoo, P. and S.K. Das, *Tribology of electroless nickel coatings – A review.* Materials & Design, 2011. **32**(4): p. 1760-1775.
18. Sudagar, J., J. Lian, and W. Sha, *Electroless nickel, alloy, composite and nano coatings – A critical review.* Journal of Alloys and Compounds, 2013. **571**(0): p. 183-204.
19. Kundu, S., S.K. Das, and P. Sahoo, *Properties of Electroless Nickel at Elevated Temperature-a Review.* Procedia Engineering, 2014. **97**(0): p. 1698-1706.
20. Mallory, G.O. and J.B. Hajdu, *Electroless plating: fundamentals and applications*. 1990, William Andrew. p. 57-98.
21. Snead, L.L., et al., *Low dose irradiation performance of SiC interphase SiC/SiC composites.* Journal of Nuclear Materials, 1998. **253**(1–3): p. 20-30.
22. Ang, C., et al., *Development of Environmental Barrier Coatings for operational conditions of SiC cladding in Light Water Reactors.* Transactions of the American Nuclear Society, Winter Meeting, Washington DC, 2015. **113**(1).

23.   Ang, C., et al., *Chromium-Based Mitigation Coatings on SiC Materials for Fuel Cladding.* Transactions of the American Nuclear Society, Summer Meeting, New Orleans, 2016. **114**(1).

24.   CCC-785, R.S.I.C.C.a.O.R.N.L.a., *Scale 6.1: A Comprehensive Modeling and Simulation Suite for Nuclear Safety Analysis and Design.* 2011, ORNL/TM-2005/39.

25.   Driscoll, M.J., *The Linear Reactivity Model for Nuclear Fuel Management.* 1990, La Grange Park, IL: American Nuclear Society.

26.   George, N.M., et al., *Neutronic analysis of candidate accident-tolerant cladding concepts in pressurized water reactors.* Annals of Nuclear Energy, 2015. **75**(0): p. 703-712.

27.   Brown, N.R., M. Todosow, and A. Cuadra, *Screening of advanced cladding materials and UN–U3Si5 fuel.* Journal of Nuclear Materials, 2015. **462**: p. 26-42.

28.   Brown, N.R., et al., *Neutronic performance of uranium nitride composite fuels in a PWR.* Nuclear Engineering and Design, 2014. **275**: p. 393-407.

29.   Kamdar, M. and R. Fisher, *Structure of Electrodeposited Chromium on Gun Steel*, in *Technical Report ARL CB TR 85036 from US Army Armament Research and Development Center*. 1985, DTIC Document: Benet Weapons Laboratory.

30.   Mandich, N.V. and D.L. Snyder, *Electrodeposition of chromium.* Modern Electroplating, 2010: p. 205-248.

31.   Martyak, N.M., et al., *Microcracks in chromium electrodeposits.* Journal of Materials Science, 1997. **32**(22): p. 6069-6073.

32.   Muthumeenal, V., et al., *Internal stress in electrodeposited chromium.* Bulletin of Electrochemistry, 1991. **7**(3): p. 124-127.

33.   Torres-Gonzalez, J., F. Castaneda, and P. Benaben, *Study of Chromium Multilayers Properties Obtained by Pulsed Current Density: Residual Stress and Microhardness.* Leonardo Electronic Journal of Practices and Technologies, 2010(17): p. 117-130.

34.   Evans, A. and J. Hutchinson, *The thermomechanical integrity of thin films and multilayers.* Acta Metallurgica et Materialia, 1995. **43**(7): p. 2507-2530.

35.   Evans, A.G., M.Y. He, and J.W. Hutchinson, *Effect of interface undulations on the thermal fatigue of thin films and scales on metal substrates.* Acta Materialia, 1997. **45**(9): p. 3543-3554.

36.   Chun, S.-Y., *Bias voltage effect on the properties of TiN films by reactive magnetron sputtering.* Journal of the Korean Physical Society, 2010. **56**(4): p. 1134-1139.

37.   Fuentes, G., et al., *Recent advances in the chromium nitride PVD process for forming and machining surface protection.* Journal of materials processing technology, 2005. **167**(2): p. 415-421.

38.   Hoy, R., J.-D. Kamminga, and G. Janssen, *Scratch resistance of CrN coatings on nitrided steel.* Surface and Coatings Technology, 2006. **200**(12): p. 3856-3860.

39.   Hoy, R., W. Sloof, and G. Janssen, *Hard dense CrN x coatings on three-dimensional objects.* Surface and Coatings Technology, 2004. **179**(2): p. 215-222.

40.   Lin, J., et al., *High rate deposition of thick CrN and Cr 2 N coatings using modulated pulse power (MPP) magnetron sputtering.* Surface and Coatings Technology, 2011. **205**(10): p. 3226-3234.

41.   O'Dell, S. and L.L. Snead, *SiC Composite Claddings with Metallic Seal Coatings for Improved LOCA Tolerance (DOE SBIR Phase I (DE-SC0011892).* 40th International Conference and Exposition on Advanced Ceramics and Composites, January 24-29, 2016.

42.   O'Dell, S., *High Strength, Oxidation Resistant Fuel Claddings for Improved Accident Tolerance*, in *SBIR Proposal Topic 19, Subtopic B*. 2014, Plasma Processes, LLC: Plasma Processes, LLC.

43.   Lewis, E.E. and W.F. Miller, *Computational Methods of Neutron Transport*. 1993, La Grange Park, IL: American Nuclear Society (1993).

44.   Box, G.E., W.G. Hunter, and J.S. Hunter, *Statistics for experimenters: an introduction to design, data analysis, and model building*. Vol. 1. 1978: JSTOR.

45.   Terrani, K.A., S.J. Zinkle, and L.L. Snead, *Advanced oxidation-resistant iron-based alloys for LWR fuel cladding.* Journal of Nuclear Materials, 2014. **448**(1): p. 420-435.

46.   Akono, A.-T. and F.-J. Ulm, *Scratch test model for the determination of fracture toughness.* Engineering Fracture Mechanics, 2011. **78**(2): p. 334-342.

47.   Bucaille, J.L., E. Felder, and G. Hochstetter, *Mechanical analysis of the scratch test on elastic and perfectly plastic materials with the three-dimensional finite element modeling.* Wear, 2001. **249**(5–6): p. 422-432.

48.   Li, J. and W. Beres, *Three-dimensional finite element modelling of the scratch test for a TiN coated titanium alloy substrate.* Wear, 2006. **260**(11–12): p. 1232-1242.

49.   Per-Lennart, L. and W. Fredrik, *On indentation and scratching of thin films on hard substrates.* Journal of Physics D: Applied Physics, 2008. **41**(7): p. 074022.

50.   Kusakabe, S., H.R. Rawls, and M. Hotta, *Relationship between thin-film bond strength as measured by a scratch test, and indentation hardness for bonding agents.* Dental Materials, 2016. **32**(3): p. e55-e62.

51.   Tabor, D., *The physical meaning of indentation and scratch hardness.* British Journal of Applied Physics, 1956. **7**(5): p. 159.

52.   Gizynski, M., et al., *Formation and subsequent phase evolution of metastable Ti-Al alloy coatings by kinetic spraying of gas atomized powders.* Surface and Coatings Technology, 2017. **315**: p. 240-249.

53.   Howard, S.J. and T.W. Clyne, *Surface preparation of titanium for vacuum plasma spraying and its effect on substrate/coating interfacial fracture toughness.* Composites, 1993. **24**(8): p. 603-610.

54.   Sabiruddin, K., J. Joardar, and P.P. Bandyopadhyay, *Analysis of phase transformation in plasma sprayed alumina coatings using Rietveld refinement.* Surface and Coatings Technology, 2010. **204**(20): p. 3248-3253.

55.   Petukhov, V., *Thermal expansion of zirconium in the solid phase.* High Temperatures-High Pressures, 2003. **35**(1): p. 15-24.

56.   Matsumoto, Y., M. Morinagat, and M. Furui, *Multiple deformation effect on the ductility of chromium.* Scripta Materialia, 1997. **38**(2): p. 321-327.

57.   Hutchinson, J.W., *Stresses and failure modes in thin films and multilayers.* Notes for a Dcamm Course. Technical University of Denmark, Lyngby, 1996: p. 1-45.

58.   Janssen, G., F. Tichelaar, and C. Visser, *Stress gradients in CrN coatings.* Journal of applied physics, 2006. **100**(9): p. 093512.

59.   Janssen, G.C.A.M., *Stress and strain in polycrystalline thin films.* Thin Solid Films, 2007. **515**(17): p. 6654-6664.

60.   Janssen, G.C.A.M., et al., *Tensile stress in hard metal films.* Applied Physics Letters, 2003. **83**(16): p. 3287-3289.

61.   Matsumoto, Y., et al., *Alloying effect of 3d transition elements on the ductility of chromium.* Scripta Materialia, 1996. **34**(11): p. 1685-1689.

62.   Lin, K.-L., et al., *Electroplating of Ni-Cr on steel with pulse plating.* Journal of Materials Engineering and Performance, 1992. **1**(3): p. 359-361.

63.   Katoh, Y. and L.L. Snead. *Mechanical properties of cubic silicon carbide after neutron irradiation at elevated temperatures*. in *Effects of Radiation on Materials: 22nd Symposium*. 2006. ASTM International.

64.   Newsome, G., et al., *Evaluation of neutron irradiated silicon carbide and silicon carbide composites.* Journal of Nuclear Materials, 2007. **371**(1–3): p. 76-89.

65.   Katoh, Y., et al., *Stability of SiC and its composites at high neutron fluence.* Journal of Nuclear Materials, 2011. **417**(1–3): p. 400-405.

66.   Ohring, M., *Materials Science of Thin Films, 2nd Edition*. 2010, Boston, 1992: Academic Press.

67.   Evans, A. and J. Hutchinson, *On the mechanics of delamination and spalling in compressed films.* International Journal of Solids and Structures, 1984. **20**(5): p. 455-466.

68.   Wiklund, U., et al., *Multilayer coatings as corrosion protection of Zircaloy.* Surface and Coatings Technology, 1996. **86–87, Part 2**: p. 530-534.

69. Cheng, T., et al., *Oxidation of fuel cladding candidate materials in steam environments at high temperature and pressure.* Journal of Nuclear Materials, 2012. **427**(1–3): p. 396-400.
70. Klueh, R.L. and D.R. Harries, *High-chromium ferritic and martensitic steels for nuclear applications.* Vol. 3. 2001: ASTM International.
71. Delabrouille, F., et al., *Effect of the chromium content on the corrosion of nickel based alloys in primary water of pressurised nuclear reactors.* Materials at High Temperatures, 2005. **22**(3-4): p. 287-292.